Angular dependence of the *pp* elastic-scattering analyzing power between 0.8 and 2.8 GeV. I. Results for 1.80–2.24 GeV

C. E. Allgower,[1] J. Ball,[2,3] L. S. Barabash,[4] P.-Y. Beauvais,[2] M. E. Beddo,[1,*] Y. Bedfer,[2] N. Borisov,[4] A. Boutefnouchet,[5] J. Bystrický,[3] P.-A. Chamouard,[2] M. Combet,[2,3] Ph. Demierre,[6] J.-M. Fontaine,[2,3] V. Ghazikhanian,[5] D. P. Grosnick,[1,†] R. Hess,[6,‡] Z. Janout,[4,§] Z. F. Janout,[6,‖] V. A. Kalinnikov,[4] T. E. Kasprzyk,[1] Yu. M. Kazarinov,[4,‡] B. A. Khachaturov,[4] R. Kunne,[2,¶] J. M. Lagniel,[2] F. Lehar,[3] J. L. Lemaire,[2] A. de Lesquen,[3] D. Lopiano,[1] M. de Mali,[3,‡] V. N. Matafonov,[4] G. Milleret,[2] I. L. Pisarev,[4] A. A. Popov,[4] A. N. Prokofiev,[7] D. Rapin,[6] J.-L. Sans,[2,**] H. M. Spinka,[1] Yu. A. Usov,[4] V. V. Vikhrov,[7] B. Vuaridel,[6] C. A. Whitten,[5] and A. A. Zhdanov[7]

[1]*HEP Division, Argonne National Laboratory, 9700 South Cass Avenue, Argonne, Illinois 60439*

[2]*Laboratoire National Saturne, CNRS/IN2P3 and CEA/DSM, CEA/Saclay, F-91191 Gif-sur-Yvette Cedex, France*

[3]*DAPNIA, CEA/Saclay, F-91191 Gif-sur-Yvette Cedex, France*

[4]*Laboratory of Nuclear Problems, JINR, RU-141980 Dubna, Moscow Region, Russia*

[5]*Physics Department, University of California at Los Angeles, 405 Hilgard Avenue, Los Angeles, California 90024*

[6]*DPNC, University of Geneva, 24 quai Ernest-Ansermet, CH-1211 Geneva 4, Switzerland*

[7]*Petersburg Nuclear Physics Institute, RU-188350 Gatchina, Russia*

(Received 1 June 1999; published 15 October 1999)

Experimental results are presented for the *pp* elastic-scattering single spin observable $A_{oono}=A_{ooon}=A_N=P$, or the analyzing power, at 19 beam kinetic energies between 1795 and 2235 MeV. The typical c.m. angular range is 60–100°. The measurements were performed at Saturne II with a vertically polarized beam and target (transverse to the beam direction and scattering plane), a magnetic spectrometer and a recoil detector, both instrumented with multiwire proportional chambers, and beam polarimeters.
[S0556-2813(99)03610-9]

PACS number(s): 13.75.Cs, 13.88.+e, 25.40.Cm

I. INTRODUCTION

For decades, nucleon-nucleon elastic-scattering and total cross section measurements have been very important to test models of the strong interaction and to provide input to calculations of proton scattering from nuclei. These experiments have progressed over time, yielding improved statistical errors, a larger variety of spin observables, and a wider energy range. These results have led to improved models of strong interactions at intermediate energies. This paper provides final results for a portion of a large experimental program to measure proton-proton elastic-scattering spin observables up to a kinetic energy of 2.8 GeV using the Saturne II accelerator at Saclay.

The analyzing power, $A_N=P$, was measured in this experiment using a polarized proton beam that scattered from a polarized proton target. If the beam, target, forward scattered, and recoil proton spin directions are denoted b,t,f,r, respectively, and if the spin observables X are defined as $X_{frbt}=(b,t;f,r)$, then the analyzing power is

$$A_N=P=A_{oono}=(N,0;0,0)=\frac{d\sigma/d\Omega(\uparrow)-d\sigma/d\Omega(\downarrow)}{d\sigma/d\Omega(\uparrow)+d\sigma/d\Omega(\downarrow)}.$$

The spin directions are defined as normal to the scattering plane or vertical (n or N), along the beam direction or longitudinal (k or L), and in the scattering plane orthogonal to the beam direction (s or $S=\vec{N}\times\vec{L}$). If the spin is not measured or the proton is unpolarized, the spin direction is denoted by a ''*o*'' or ''0.'' For identical beam and target particles, $A_{oono}=A_{ooon}$, allowing the beam polarization to be determined if the target polarization is known. The measured asymmetries were averaged over either the beam or the target polarization states to obtain A_N. Values of the two-spin observable, $A_{oonn}=A_{NN}=C_{NN}$, were measured at the same time as the results in this paper, and will be published separately. The nucleon-nucleon formalism is described in further detail in Ref. [1].

The A_N results from the first part of this experiment are described here; the remainder are presented in the accompanying paper [2]. A comparison to previously published data and to phase-shift predictions is made. Results at some beam energies were measured in both parts of this experiment, and these are compared in Ref. [2]. In addition, the energy dependence of A_N at two c.m. angles and of $dA_N/d\theta$ at a third angle θ are shown in Ref. [2]. These analyzing power data are important for deriving values of other spin observables involving polarized proton beams, such as for proton scatter-

*Present address: Data Ventures, LLC, Los Alamos, NM 87544.

†Present address: Department of Physics and Astronomy, Valparaiso University, Valparaiso, IN 46383.

‡Deceased.

§Present address: Faculty of Nuclear Sciences and Physical Engineering, Czech Technical University, Břehová 7, 11519 Prague 1, Czech Republic.

‖Present address: Computing Center of the Czech Technical University, Zikova 4, 16635 Prague 6, Czech Republic.

¶Present address: Institut de Physique Nucléaire IN2P3, F-91400 Orsay, France.

**Present address: Centrale Themis, F-66121 Targasonne, France.

ing from hydrogen or nuclei. For example, at the energies of these measurements, the beam polarization in an experiment is usually determined by elastic scattering of the beam from a liquid hydrogen or CH_2 target using known values of A_N.

The apparatus used in this experiment is described in Sec. II, and details of the data analysis are given in Sec. III. The results are presented in Sec. IV and the accompanying paper [2]; additional details can be found in Ref. [3]. Preliminary values from measurements of A_{oonn} obtained at the same time as some of the data in this paper were described in Ref. [4], however improved beam polarization values and cuts on the data have been employed in the data analysis. Other results from these experiments are presented in Refs. [5–8].

II. EXPERIMENTAL APPARATUS

The experiment was performed with a polarized proton beam incident on a frozen-spin polarized proton target during four run periods spread over a three year time span. The first two run periods are described in this paper, and the last two in the accompanying paper [2]. Each run period was 10–14 days in duration, during which measurements were made at a number of energies. Some changes were made to the apparatus for different run periods, as described in the following subsections and Ref. [2].

A. Polarized beam

The polarized beam was produced in an atomic beam-type polarized ion source, called Hyperion [9–14]. The beam polarization direction was approximately horizontal sideways after extraction from Hyperion. Two rf transition cavities were used for the proton beam in this source, giving four possible polarization states depending on whether each cavity was on or off. These will be designated ''0_+'' (off-off, state 1), ''$-$'' (on-off, state 2), ''$+$'' (off-on, state 3), and ''0_-'' (on-on, state 4). The 0_+ and 0_- states were nominally unpolarized, $+$ was vertically up at the entrance to Saturne II, and $-$ was vertically down. For run period I, most of the data were collected with only the $+$ and $-$ polarization states alternating each beam pulse, but the first three energies also had the 0_+ state. For the other run periods, usually all four polarization states were used, with the 0_+ and 0_- states used during half the number of beam pulses as the $+$ and $-$ states in the pattern 0_+, $-$, $+$, 0_-, $-$, $+$, 0_+, $-$, $+$, 0_-,… .

A special set of measurements [15] of the Hyperion ion source performance was made subsequent to the experiments described in this paper and in Ref. [2]. In addition to the polarized beam, an unpolarized beam was required to determine the instrumental asymmetry in a polarimeter. With this information, the polarizations of the individual Hyperion spin states could be determined. It was shown that the 0_+ and $+$ states were both ''positively'' (contained more protons with spin $+$ than with spin $-$), and the 0_- and $-$ states were both ''negatively'' polarized. In addition, the magnitudes of the 0_+ and 0_- states were equal, small, and nonzero, and of the $+$ and $-$ states were also equal in magnitude within statistical errors. Finally, these results were found to be relatively insensitive to the ion source operating conditions near the nominal values of rf power, hexapole current, and electrostatic mirror voltage. Additional details are presented in Sec. III B and in Ref. [15].

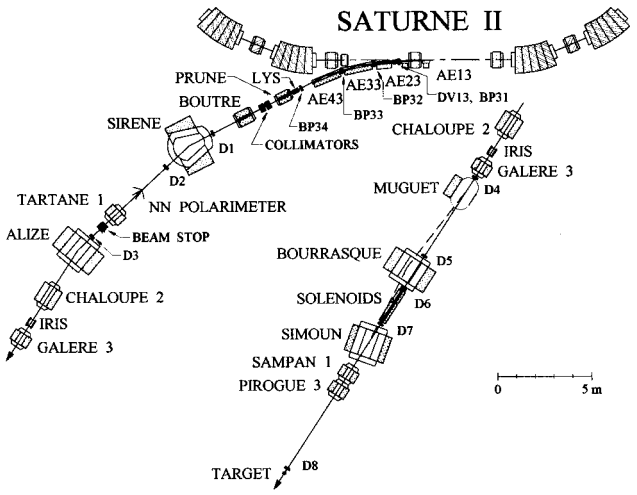

FIG. 1. Layout of the SD3 and nucleon-nucleon beamline, showing a portion of the Saturne II accelerator. The dipole magnets all had vertical fields except Dv13, Lys, and Iris. Beam profile chambers BP32–BP34 and D1–D8 are also shown. The magnets Muguet to Simoun were used to produce a longitudinally polarized beam along the dashed line. Magnets Chaloupe 2, Iris, and Galère 3 are repeated for the two sections of the figure, with the beginning of the beamline shown on the left and the rest on the right. The dipole magnet AE13 is composed of two parts on opposite sides of a Saturne magnet.

After the polarized ion source, the beam polarization was rotated into the vertical direction by a solenoid. The beam was then accelerated in the Mimas booster ring and the Saturne II accelerator. The beam polarization remained vertical, but was flipped 180° during acceleration through each of several strong depolarizing resonances in Saturne II. Once the beam particles attained the desired energy, their orbits were distorted and the particles were slowly extracted via a septum magnet to the SD3 beamline center; see Fig. 1. The vertical-field dipole magnets AE13–AE43 were used to tune the beam successively onto the beam profile monitors BP32–BP34 and finally onto D1. These beam profile monitors were removed remotely when the tuning was complete. The large bending magnet, Sirène, was used to select the beam line either for the spectrometer SPES IV, a test beam area, or the nucleon-nucleon experimental area. For a few energies in run period I, copper absorbers were installed upstream of the AE13 magnet at a beam energy of 2240 MeV to slightly degrade the beam energy. Such absorbers are not expected to depolarize the beam. This occurred near an energy corresponding to a depolarizing resonance in the Saturne accelerator. The beam intensity was kept significantly lower than the maximum available so as to prevent rapid radiation damage to the polarized target material and to allow reasonable computer live time.

The nucleon-nucleon beam line is also shown in Fig. 1, and was capable of providing proton beams with longitudinal (L), transverse horizontal (S), or transverse vertical (N)

spin directions at the target. It changed somewhat since previous pp scattering experiments [16–20]. Located after Sirène was a 56 mm diameter steel collimator, the SD3 polarimeter [21], and a beam stop, followed by the dipole magnet Alizé. Sirène was tuned using the narrow target in the SD3 polarimeter by maximizing the detected scattered events, and was checked with the beam profile monitor D3. Finally, the current in Alizé was set by maximizing the scattered events detected from the polarized target and the narrow monitor target immediately downstream of the polarized target. The beam profile monitor D8 was used to confirm the Alizé setting. The dipole magnets Muguet, Bourrasque, and Simoun, and the superconducting solenoidal magnets, were required for operation of polarized neutron beams and to produce longitudinally polarized proton beams; they were not used in these experiments. Several small vertical steering magnets (Dv13, Lys, Iris) were frequently off or were used to make very small vertical bends in the beam. The quadrupole magnet currents were approximately scaled with beam momentum. The beam profile monitors D2–D7, and often D8, were removed remotely after the beam tuning.

The typical size of the beam at the profile monitor D8, near the polarized target, was ~ 20 mm in diameter, and the typical beam polarization was 0.6–0.8. The position of the beam at the downstream polarimeter (Sec. II B) was measured at most energies in run periods III and IV, and was found to change by ± 2.0 cm. It is estimated that this change corresponds to a variation in the incident beam angle at the polarized target of ± 3.1 mrad or less. This variation could cause a systematic error in the c.m. angle, and would appear as a zero crossing of $P = A_{oono}$ at an angle different from 90°; see Sec. III E.

B. Beam polarimeters

Three relative beam polarimeters were used to monitor the vertical (N-type) and horizontal (S-type) transverse components of the beam polarization. These were the SD3 polarimeter located near the Sirène magnet, the target region or ''antipolarimeter'' situated 2.50 m upstream of the polarized target, and the downstream or ''Gatchina'' polarimeter whose target was 6.54 m downstream of the polarized target, described in detail in Ref. [2]. They measured the vertical, horizontal, and vertical components of the beam polarization, respectively. The downstream polarimeter was partially installed and tested in run period II, but was fully operational only during run periods III and IV. Scaled quantities from these polarimeters were used to monitor the beam polarization online and offline; see Sec. III B.

The SD3 polarimeter has been used for many past experiments and is described in detail in Ref. [21]. Its target was either a carbon or CH_2 block, 2 mm wide, 15 mm high, and 5 mm thick along the beam direction; the width was somewhat narrower than the beam spot. There were four arms in the horizontal plane with two scintillation counters in each arm. Two arms, consisting of counters SP_1 and SP_2, and SP_5 and SP_6, were symmetrically located on opposite sides of the nominal beam line to detect the forward scattered protons. They were situated at laboratory angles of 13.9° for the measurements described in this paper. The other two arms were also located on opposite sides of the beam, and contained scintillation counters SP_3 and SP_4, and SP_7 and SP_8. These arms detected the recoil protons, and their laboratory angles could be changed remotely. By adjusting the angles, these arms could be positioned to be ''on'' or ''off'' pp elastic-scattering kinematic conditions with respect to the forward arms. The recoil angles of the polarimeter arms were not adjusted for each energy, rather they remained fixed over a range of energies. At each energy during normal data taking, both carbon and CH_2 target data were typically collected, each with ''on'' and ''off'' kinematic recoil angles. Fourfold coincidences $L_c = SP_1 \cdot SP_2 \cdot SP_3 \cdot SP_4$ and $R_c = SP_5 \cdot SP_6 \cdot SP_7 \cdot SP_8$ were generated electronically and scaled. Accidental coincidences were also scaled.

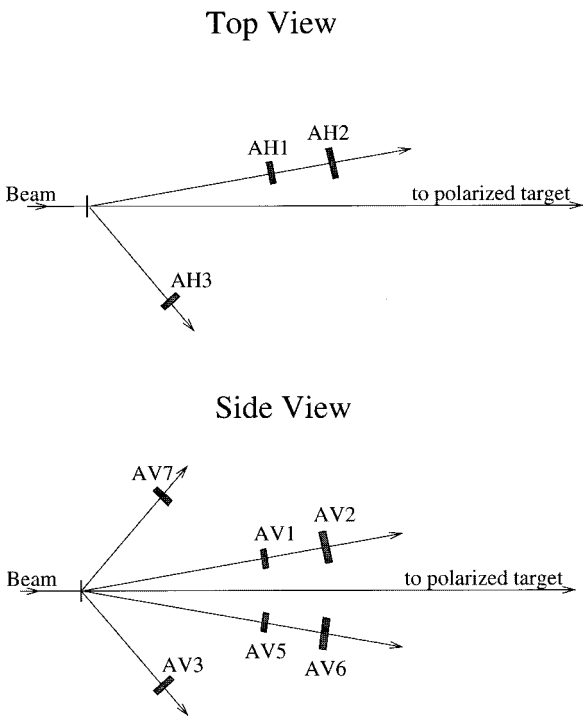

FIG. 2. Top and side views of the target region polarimeter (not to scale) showing the location of the scintillation counters.

Another pair of symmetric arms viewed the SD3 polarimeter target vertically, and consisted of scintillation counters PH_1 and PH_2, and PB_1 and PB_2. The coincidences $PH = PH_1 \cdot PH_2$ and $PB = PB_1 \cdot PB_2$ and their accidentals were also scaled. These quantities were sensitive to any S-type component of the beam polarization, but were mainly used for beam intensity monitoring.

The target-region polarimeter (see Fig. 2) consisted of six arms. Two vertical arms were symmetrically located above and below the nominal beam line at $\sim 13°$, and detected forward-scattered protons. They consisted of scintillation counters AV_1 and AV_2, and AV_5 and AV_6. The corresponding conjugate arms contained a single scintillation counter each, AV_3 and AV_7. The other two arms were in the horizontal plane and corresponded to a beam-left forward arm (AH_1,AH_2) and its conjugate recoil arm (AH_3) on beam-right. The dimensions of the counters and distances to the

TABLE I. Scintillation counter sizes and distances to the plexiglass target for the target region polarimeter. For locations, see Fig. 2.

Counter	Height (mm)	Width (mm)	Thickness (mm)	Distance to target (cm)
AV1, AV5	90	40	3	55
AV2, AV6	125	60	4	75
AV3, AV7	240	60	5	44
AH1	90	40	3	63
AH2	125	60	4	79
AH3	240	60	5	28

polarimeter target are given in Table I. Double and triple coincidences and accidentals were generated with standard electronics and scaled ($AV_1 \cdot AV_2 \cdot AV_3$, etc.).

The target for the target-region polarimeter was 5-mm-thick plexiglass with transverse dimensions much larger than the beam spot. Thus, the number of scattering events detected by this polarimeter was not very sensitive to changes in beam position compared to the other two polarimeters. No target changes were made during these experiments. However, manual adjustments to the recoil arm angles were made occasionally, depending on the beam energy. The main functions of the target-region polarimeter were (1) to set the beam-line solenoid currents to produce a 90° spin precession when a *S*-type beam was desired, and (2) to serve as a beam-intensity monitor. For the second function, the relative insensitivity to beam position changes was an advantage. The beam intensity normalization used the quantity $AV = \sqrt{AV_{12} \cdot AV_{56}}$, where the coincidence signals $AV_{12} = AV_1 \cdot AV_2$ and $AV_{56} = AV_5 \cdot AV_6$ were formed with standard electronics modules; accidentals were subtracted from these coincidences before computing AV.

C. Polarized target

The polarized proton target (PPT) used for these measurements is described in Refs. [22,23]. It included a vertical dilution refrigerator, a superconducting polarizing solenoid, two superconducting holding field magnets, a microwave system, a nuclear magnetic resonance (NMR) system to measure the polarization, a data acquisition system to monitor the target performance, and associated equipment. Data collected for the different target polarization states were typically separated in time by periods of 3–40 h. Changes in detector performance over these periods could have led to false asymmetries. Therefore, considerable effort was made to search for such changes in the data analysis; see Sec. III E.

Microwaves were used to polarize the target material via the technique of dynamic nuclear polarization [24]. The target material was located at the center of the highly uniform 2.5 T magnetic field of the polarizing solenoid, and was at a temperature about 0.3 K during the polarization. After the polarizing process was complete, the microwaves were turned off, and the target temperature reduced to as low as 40 mK, thus ''freezing in'' the polarization, and initiating the frozen-spin mode of the target's operation. The field of one of the holding magnets was then turned on and increased, while the polarizing solenoid field was decreased, as described in Ref. [22]. The holding field at the target center was 0.33 T. The holding magnets were located above or upstream of the target, and did not interfere with the incoming beam. The polarizing solenoid was completely lowered from around the target material before the beam was brought back into the experimental area.

The target material was located in a cylindrical container of Voltalef. For run period II, the diameter was 20 mm and the length was 44 mm, while for the other three run periods the width, height, and length were 40 mm×49 mm×35 mm, respectively. A mixture of 95% pentanol and 5% water, doped with EHBA–Cr^V, was used as the target material; pentanol–1 ($CH_3CH_2CH_2CH_2CH_2OH$) was used in run period II and the second part of run period I, and pentanol–2 ($CH_3CH_2CH_2CHOHCH_3$) in the first part of run period I. Different target materials were used in an attempt to maximize the target polarization while achieving long polarization decay times. The materials were in the form of small ($\sim$2.0 mm) diameter glassy beads, made by rapid freezing of liquid drops in liquid nitrogen. The bead diameters varied from bead to bead by about $\pm$0.2 mm, with target filling factors 67–70 %.

The absolute target polarization was determined by a comparison of the NMR signals in the polarized state and when the target material was in thermal equilibrium near 1 K, as measured by the current in two ruthenium oxide resistors, calibrated to $\pm$0.01 K [23]. The thermal equilibrium measurements were made (with microwaves turned off) immediately before the pentanol-2 runs and twice at the end of the pentanol-1 runs in period I, and at both the beginning and end of run period II. The target polarization measurements were usually performed before entering and after leaving the frozen-spin mode of operation. (For one case in run period I and another in run period II, the target polarization after the frozen-spin mode for one target state at 2035 and 2095 MeV could not be recorded because of instrumental problems. This led to larger errors at these energies; see Sec. III E.) Initial values of the proton target polarization before entering frozen spin mode were generally in the range 0.65–0.85, and typical polarization decay times ($1/e$) while in the frozen-spin mode were $\sim$400 h. Target polarizations for a given run were calculated from the known starting and ending times for the run, and the values and times when the polarization was measured, assuming a uniform exponential decay. The estimated relative systematic uncertainty on the absolute target polarization is $\pm$3%, primarily from the absolute temperature determination during the thermal equilibrium measurements.

A solid CH_2 target, 20 mm in diameter by 10 mm along the beam, was located about 17 cm downstream from the center of the polarized target in run periods II, III, and IV. Elastic-scattering events from this target provided useful checks of systematic errors in the data, though the acceptance of the detectors was somewhat reduced compared to the events from the polarized target [6]. In run period I, a ^{6}LiD or ^{7}LiH target of thickness 25 mm was used instead of the CH_2 target. Events from these ''monitor'' targets were

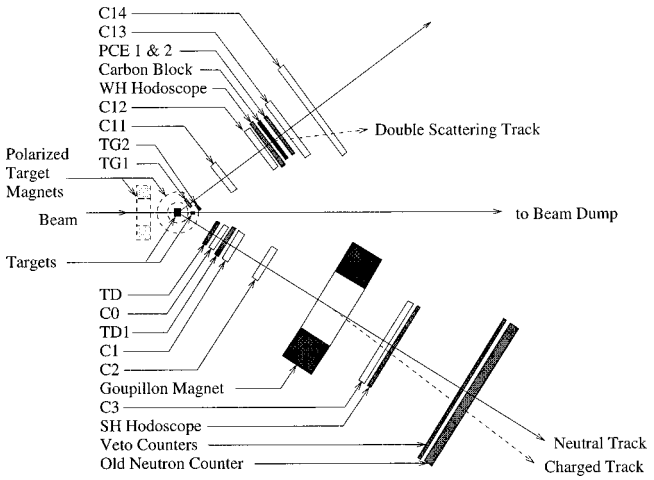

FIG. 3. Experimental layout showing the magnetic spectrometer and polarimeter arms and associated detectors (not to scale). The detectors are described in the text.

also used for beam tuning, as described in Sec. II A.

D. Detectors

A top view of the experimental detectors is shown in Fig. 3. Particles scattered from the PPT were detected by a two-arm array consisting of a magnetic spectrometer and a carbon rescattering polarimeter. The spectrometer arm included two trigger scintillation counters (TD1, TD), four multiwire proportional chambers (MWPC's–C0,C1,C2,C3), a large-aperture analyzing magnet (Goupillon), a scintillation counter hodoscope (SH) made of 12 vertical counters, and a neutron counter array with 15 horizontal bars and four associated charged particle veto counters. The polarimeter arm contained four trigger scintillation counters (TG1,TG2, PCE1,PCE2), four MWPC's (C11,C12,C13,C14), a scintillation counter hodoscope (WH) with six vertical counters, and an 8-cm-thick carbon block for rescattering. Many details about the apparatus are given in [3,25,26].

Information about the MWPC's, such as the useful dimensions, number of instrumented wires per plane, number of planes, wire spacing, and distances of the chamber centers from the PPT are given in Table II. Most of these values are similar to the results in Table I of Ref. [26]. However, a new chamber C0 with LeCroy PCOS3 readout was installed before these spin measurements, and this required a modified distance to chamber C1. The chamber C0 was not fully functional in run period I, and its data were excluded from the analysis for those runs; data from C0 were used in the other three run periods. Information from the rescattering of protons in the carbon [7] was not used for the results given here, so data from chambers C13 and C14 were ignored in the present analysis.

The center of the spectrometer magnet, Goupillon, was positioned 320 cm downstream of the PPT. Its aperture was 150 cm horizontally and 60 cm vertically, and its maximum field integral was 0.74 T m. The magnetic spectrometer arm was nominally centered at 32° lab from the beam for all measurements in this paper, and it was not moved from the beginning of run period II until the end of run period IV. This precludes systematic shifts in the measured laboratory angle due to alignment of the magnetic spectrometer.

The neutron counter array [26] in the spectrometer arm was used for triggering on protons. Each scintillator bar was viewed by two photomultipliers, and had dimensions 8 cm high, 3 m long, and 20 cm thick. The time of flight over the 6.6 m flight path from the PPT to the neutron counters was recorded for each photomultiplier signal. The difference in times between the signals from the two photomultipliers for each bar determined the horizontal position where the particle hit the bar. Four large veto counters for charged particles were located immediately upstream of the neutron counter array. Each veto counter was a plastic scintillator viewed by a single photomultiplier.

E. Trigger electronics

The experimental trigger was formed with information from scintillation counters and hodoscopes, but not MWPC's. All photomultiplier signals were discriminated and transformed into logic signals, either by leading-edge or constant-fraction discriminators. The signals from the dis-

TABLE II. Characteristics of the MWPC's. *X* represents the number of instrumented vertical wires, and *Y* indicates the horizontal wires for all chambers. *U* corresponds to wires inclined at 14.36° from the vertical for chambers C1–C14, and *U* and *V* correspond to wires inclined at +27.88° and −28.22° for C0. The useful horizontal and vertical dimensions in mm of the chambers are presented, and the distance from the center of the PPT to the center of the MWPC is also given.

MWPC	Number of planes	Wire Spacing (mm)	*X*	*Y*	*U*	*V*	Horiz.	Vert.	Distance from PPT (mm)
C0	4	2.0	256	128	297	297	512	256	928
C1	3	3.0	216	128	248		648	384	1210
C2	3	2.0	356	200	392		712	400	1802
C3	3	2.0	888	436	948		1776	872	4606
C11	3	2.0	292	136	312		584	272	1120
C12	3	2.0	440	252	484		880	504	1862
C13	3	2.0	628	440	720		1256	880	2600
C14	3	2.0	1012	440	964		2024	880	3340

criminators, corresponding to the top and bottom photomultipliers for each counter in the WH and SH hodoscopes, entered mean-timer circuits. The mean-timers minimized timing variations caused by different positions in these counters where the incident particles hit. Logical OR's of the signals from the mean timers were formed for all SH hodoscope counters (ΣSH) and all WH counters (ΣWH).

Two pretriggers were generated for these experiments. One provided the trigger for pp elastic-scattering events due to scattering in the polarized target, defined as

$$TPP = TD1 \cdot \sum \text{SH} \cdot TG1 \cdot \sum \text{WH},$$

and the other for events scattered in the CH_2 target downstream of the polarized target,

$$MPP = TD1 \cdot \sum \text{SH} \cdot TG2 \cdot \sum \text{WH}.$$

Note that the CH_2 target was mounted directly to the $TG2$ scintillation counter. The fraction of pretriggers corresponding to MPP was typically 5–15 %, with the remainder being TPP events.

The final or master trigger was a coincidence between an OR of the neutron counters (used to detect protons), and either TPP or MPP. Only one or two adjacent neutron bars were allowed to have a signal for the master trigger. The master trigger signal: (a) generated a BUSY signal to prevent subsequent triggers until the readout was complete, (b) made the gates to latch the SH, WH, and pretrigger information, (c) gave the common STOP signal for the time-to-digital converters, (d) formed the gate for the analog-to-digital converters for the neutron counters, (e) generated the latch signals for the MWPC's, and (f) initiated the event readout.

Many quantities were scaled, including various polarimeter coincidences and accidentals, and signals in the trigger, such as $TD1$, ΣSH, and TPP. The scalers were gated with either the Saturne spill gate or with the spill gate inhibited by the computer BUSY signal. The Saturne spill gate was started with a signal from the accelerator, and corresponded to the beam extraction time. Some quantities were scaled with both gates in order to measure the deadtime associated with the read-in of the data. Scaled quantities with the spill gate plus the computer BUSY signal were used for beam normalization of the elastic-scattering data. Further details of the trigger electronics are given in Refs. [3,25,26].

F. Data acquisition system

During run period I, the data acquisition system consisted of a special CAMAC crate controller [Controleur Auxiliaire de Chassis (CAC) [27]]. The CAC module was based on a Motorola 68000 microprocessor, and read data from modules in a single CAMAC crate. It was used for event-by-event data acquisition, some histogramming, and online diagnostics. An online computer, Isadora, read the individual events from the CAC and the scalers from other CAMAC crates at the end of each spill, and wrote these data to 9-track magnetic tapes. This computer, homebuilt at Saclay and based on a Motorola 68010 chip, also displayed the histograms, started and ended runs, and printed scaler data and the results of online diagnostics of the chamber performance.

This system was replaced before run period II by a Sun Sparc1 card in a VME crate running VxWorks data acquisition software, and a Sun SparcStation 1+ computer. The new system had more than double the data acquisition rate of the earlier system. The data were transferred from the Sparc1 card to the Sun computer, and then to 8 mm Exabyte magnetic tapes. Scaler and diagnostic data were also saved to disk. The online software allowed extensive monitoring of hardware performance, which had been limited in the older system by available memory and the difficulty of programming the CAC. For both data acquisition computers, the typical live time was maintained between 30 and 60 %.

The data from all run periods were eventually copied to 8 mm Exabyte magnetic tapes for later analysis. The data formats were similar from the two data acquisition systems, but one block of variable length was written per spill in run period I, and two fixed-length blocks of data were written in run period II. However, problems were encountered with how some of the information was written to tape. As a consequence, considerable effort was required to recover and/or repair the badly written raw data. Eventually about 95 and 83% of the data from run periods I and II, respectively, were recovered. The total raw data recovered for these run periods corresponded to approximately 3×10^7 events for each period, and 6 and 9 Gbytes, respectively.

III. DATA ANALYSIS

The data analysis occurred semi-independently in two separate locations, Saclay and Argonne. Much of the offline analysis software was in common, but there were also important differences. The results of the two analyses are combined for the final values presented, and the quoted uncertainties contain a contribution from the difference between the two sets of values. In both cases, equations for the observed yields of elastic-scattering events were solved for the spin observables A_N and A_{oonn}. The two analyses used somewhat different cuts, and had different sensitivities for some types of systematic errors. However, the good agreement of the derived $A_N = A_{oono} = A_{ooon}$ values suggests these systematic effects are generally small. Some additional details may be found in Refs. [3,25].

There were several steps in the data analysis. The first step analyzed the scaler values read at the end of each spill. Spills with bad or unusual experimental conditions or without beam were identified and removed with cuts. In some cases, problems with the signals being scaled or with the operation of the scalers were uncovered; no cuts were made for these conditions unless these scaled quantities were crucial for the determination of A_N. In general, the two semi-independent analyses used somewhat different cuts. A special case of the scaler analysis was the evaluation of

polarimeter scaler data. Various asymmetries and ratios were computed, and this information was used in the evaluation of the elastic scattering data.

The next step dealt with the elastic scattering events. The scintillator hodoscope, neutron counter, and MWPC data were decoded to give the positions of the particle tracks. One of the two analyses searched extensively for changes in relative efficiencies for hodoscope and neutron counters, wire chamber planes, and individual wires. Also, searches were made for changes in the distribution of the number of times wires were hit as a function of the polarized beam state. Based on this information, cuts to remove counters, individual wires, or wire chamber planes were determined. The other analysis did less extensive studies, but also removed data from certain trigger counters or wire chamber planes with similar types of cuts at some energies.

After the removal of information from certain counters, wires, or wire planes, and of spills by the preceeding cuts, the remaining data were analyzed. Particle positions in the MWPC's and trajectories were computed. The momentum of the particle in the magnetic spectrometer arm and other kinematic quantities were calculated. Cuts were made to remove nonelastic events. The remaining backgrounds and the number of elastic-scattering events were then estimated. The software for this last step was nearly identical for the two data analyses, but again the individual cuts within each analysis varied.

The final step took the number of elastic events for each of the polarized beam and target states and derived the spin observables as a function of the c.m. angle. Two slightly different schemes were used to determine the spin observables and to search for any remaining hardware problems in the data.

A. Scaler data

The first step in the data analysis was to read the scaler information from the data tapes. Histograms and plots as a function of spill number (i.e., time) were generated for scaler quantities per spill or ratios of two scalers. The goal was to search for and eliminate spills where sizable changes occurred in experimental conditions. This would keep the efficiencies of the apparatus as constant as possible at each energy, reducing the effects of certain types of systematic errors. For example, at times sizable changes in beam intensity, beam position, computer live-time, or trigger rate from some scintillation counters were observed.

The plots and histograms for all runs at each energy were visually inspected. From this information, cuts on the data were then determined, and all events within spills that failed at least one of these cuts were eliminated from the later stages of the data analysis. As much as possible, the applied cuts were identical for *both* polarized target states at each energy. These cuts typically rejected less than 5% of all spills for both target states and all four beam polarization states at an energy. Some cuts were applied at only one or two energies, in response to specific hardware problems.

Examples of plots and histograms with cuts at some energies included: (a) the relative beam intensity at the SD3 polarimeter, $\sqrt{PH \cdot PB}$, or near the polarized target, AV; (b) the trigger rates, such as TPP/AV and $TPP/\Sigma\mathrm{SH}$; (c) the computer live time from the ratio of scaler values with the two gates; (d) the horizontal beam position or beam angle at the SD3 polarimeter from SP_{12}/SP_{56}, where the coincidence signals $SP_{12}=SP_1 \cdot SP_2$ and $SP_{56}=SP_5 \cdot SP_6$ were generated electronically; and (e) the vertical beam position or beam angle at the target-region polarimeter, AV_{12}/AV_{56}. Other histograms and plots included ratios such as $\mathrm{SH}_i/\Sigma\mathrm{SH}$ or $\mathrm{WH}_j/\Sigma\mathrm{WH}$ as a function of spill number.

This step in the data analysis went very quickly because of the small fraction of the data on the tapes that the scaler values represented. However, it was quite important to minimize systematic errors that could be introduced by different detector inefficiencies during runs for the two polarized target states at each energy. Also, some scaler ratios were very sensitive to changes in the beam tune; some of these changes could have caused systematic errors in the data. Such systematic errors will be discussed further in Sec. III E.

B. Polarimeter

Scaler data from the polarimeters were analyzed independently of the elastic scattering measurements. The results of the polarimeter analysis yielded two important constraints that applied to the elastic analysis, as described further in Sec. III D. One result is that the relative magnitudes of the four beam polarization states are consistent with being constant, independent of energy and time. Based on this result, it will be assumed in further analysis that this is the case. The other type of constraint is the value of the ratio of these polarizations for the two *target* polarization periods at each energy.

One of the most important results was derived from the scalers for the two pairs of left and right arms of the SD3 polarimeter. The input data included the fourfold coincidences $L_c=SP_1 \cdot SP_2 \cdot SP_3 \cdot SP_4$ and $R_c=SP_5 \cdot SP_6 \cdot SP_7 \cdot SP_8$ and the associated accidentals $L_{\mathrm{acc}}=SP_1 \cdot SP_2 \cdot (SP_3 \cdot SP_4)_{\mathrm{del}}$ and $R_{\mathrm{acc}}=SP_5 \cdot SP_6 \cdot (SP_7 \cdot SP_8)_{\mathrm{del}}$ as described in Sec. II B. These scalers were enabled by the Saturne spill gate, and were read after each spill.

For each experimental run of 1–2 h duration, the polarimeter scalers were summed and the accidentals subtracted, giving eight quantities $(L_1,L_2,L_3,L_4,R_1,R_2,R_3,R_4)$ for the four beam polarization states and the left and right polarimeter coincidences. In some runs, there were only three or two polarization states, with either the ''0_-'' or both the ''0_+'' and ''0_-'' states missing.

It was assumed that there was no beam position change at the polarimeter target correlated with the beam polarization state. Such motion was not expected, and was found to be less than 0.1 mm (unmeasurably small) in a test at one energy. Then the eight quantities can be written as

$$L_1=L_{0+}=B_1 \cdot C \cdot d\Omega_L \cdot (1+P_1 \cdot A_L),$$

$$R_1 = R_{0+} = B_1 \cdot C \cdot d\Omega_R \cdot (1 - P_1 \cdot A_R),$$
$$L_2 = L_- = B_2 \cdot C \cdot d\Omega_L \cdot (1 - P_2 \cdot A_L),$$
$$R_2 = R_- = B_2 \cdot C \cdot d\Omega_R \cdot (1 + P_2 \cdot A_R),$$
$$L_3 = L_+ = B_3 \cdot C \cdot d\Omega_L \cdot (1 + P_3 \cdot A_L),$$
$$R_3 = R_+ = B_3 \cdot C \cdot d\Omega_R \cdot (1 - P_3 \cdot A_R),$$
$$L_4 = L_{0-} = B_4 \cdot C \cdot d\Omega_L \cdot (1 - P_4 \cdot A_L),$$
$$R_4 = R_{0-} = B_4 \cdot C \cdot d\Omega_R \cdot (1 + P_4 \cdot A_R). \quad (1)$$

The integrated beam intensity for each beam polarization state j is B_j, the products of effective solid angle times efficiency are represented by $d\Omega_L$ and $d\Omega_R$, and the polarimeter analyzing powers are A_L and A_R. The polarizations (after extraction of the beam from Saturne II) for each state i are P_i, and the cross section and target thickness are contained in the constant C. The values of P_i are all expected to be positive (or negative if an odd number of strong depolarizing resonances were crossed during acceleration), based on details of the ion source operation. Typically, $P_2, P_3 \sim 0.6$–0.9 and $A_L, A_R \sim 0.1$–0.3 for these experiments.

The quantities in Eqs. (1) can be combined in various ways to derive information on the parameters. For the case of only two beam polarization states ($-, + = 2,3$) with nearly equal integrated beam intensity and polarization magnitudes ($B_2 \simeq B_3$, $P_2 \simeq P_3$), the following expressions can be determined:

$$\epsilon_{23} = \frac{1}{2} \cdot (P_2 + P_3) \cdot A + O(\epsilon^3) = \frac{\sqrt{L_3 R_2} - \sqrt{L_2 R_3}}{\sqrt{L_3 R_2} + \sqrt{L_2 R_3}}, \quad (2a)$$

$$S_{23} = 2 \cdot (B_2 + B_3) \cdot C \cdot d\Omega + O(\epsilon^3) = L_2 + R_2 + L_3 + R_3, \quad (2b)$$

$$\epsilon_{B32} = \frac{B_3 - B_2}{B_3 + B_2} + \frac{1}{2} \cdot (P_2 + P_3) \cdot A \cdot \epsilon_A + O(\epsilon^3) = \frac{\sqrt{L_3 R_3} - \sqrt{L_2 R_2}}{\sqrt{L_3 R_3} + \sqrt{L_2 R_2}}, \quad (2c)$$

$$\epsilon_{\Omega 23} = \epsilon_\Omega + \frac{1}{2} \cdot (P_3 - P_2) \cdot A + O(\epsilon^3) = \frac{\sqrt{L_2 L_3} - \sqrt{R_2 R_3}}{\sqrt{L_2 L_3} + \sqrt{R_2 R_3}}, \quad (2d)$$

where A and $d\Omega$ are the left-right averages, $A = (A_L + A_R)/2$ and $d\Omega = (d\Omega_L + d\Omega_R)/2$. Physically, ϵ_{23} is the mean beam polarization multiplied by the average polarimeter analyzing power, S_{23} is related to the spin-averaged count rate, ϵ_{B32} is dominated by the asymmetry in beam intensity, and $\epsilon_{\Omega 23}$ is primarily the asymmetry in the product of polarimeter solid angle and detection efficiency. The following small quantities are presumed to be all about the same order of magnitude (ϵ):

$$P_i \cdot A,$$
$$\epsilon_A = (A_L - A_R)/(A_L + A_R),$$
$$\epsilon_\Omega = (d\Omega_L - d\Omega_R)/(d\Omega_L + d\Omega_R),$$
$$(B_3 - B_2)/(B_3 + B_2),$$
$$(P_3 - P_2)/(P_3 + P_2).$$

It should be noted that the sum of the polarization magnitudes $(P_2 + P_3)$ always occurs as a product with the average analyzing power A. The difference $(P_3 - P_2) \cdot A$ occurs only with ϵ_Ω, the asymmetry in the effective solid angle and efficiency for the two arms. Thus, it is not possible to determine P_2 and P_3 separately without independent knowledge of ϵ_Ω.

The addition of another beam polarization state does not allow the separate determination of $\epsilon_A, \epsilon_\Omega$, or the difference $(P_3 - P_2)$, either. For example, the new information allows the calculation of

$$\epsilon_{21} = \frac{1}{2} \cdot (P_1 + P_2) \cdot A + O(\epsilon^3),$$
$$S_{12} = 2 \cdot C \cdot d\Omega \{(B_1 + B_2) + A \cdot (\epsilon_A + \epsilon_\Omega) \cdot (B_1 P_1 - B_2 P_2)\} + O(\epsilon^3).$$

For this experiment, $2B_1 \simeq B_2, B_3$ because the ''0+'' state was run only about half the number of spills as the + or − beam polarization states. In addition, $P_1 \ll P_2, P_3$, leading to the extra term in S_{12}. All other expressions, such as ϵ_{13}, S_{13}, ϵ_{B12}, $\epsilon_{\Omega 13}$, etc., can be written in terms of Eqs. (2), ϵ_{21}, and S_{12}. In particular, to order ϵ^3,

$$\epsilon_{13} = \epsilon_{23} - \epsilon_{21} = \frac{1}{2}(P_3 - P_1) \cdot A + O(\epsilon^3),$$
$$\epsilon_{\Omega 12} = \epsilon_{\Omega 23} - \epsilon_{13},$$
$$\epsilon_{\Omega 13} = \epsilon_{\Omega 23} + \epsilon_{21},$$
$$S_{13} = S_{12} + S_{23} \cdot (\epsilon_{B32} + \epsilon_{23} \cdot \epsilon_{\Omega 23}),$$
$$\epsilon_{B12} = (S_{13} - S_{23})/S_{12} - \epsilon_{21} \cdot \epsilon_{\Omega 12},$$
$$\epsilon_{B31} = (S_{23} - S_{12})/S_{13} - \epsilon_{13} \cdot \epsilon_{\Omega 13}.$$

A similar situation applies for the case when the fourth beam polarization state is added; again the differences $(P_3 - P_2)$ and $(P_1 - P_2)$ cannot be determined independently of ϵ_Ω.

However, the ratios of the sums of polarizations could be found. The quantities

$$R_{123} = \epsilon_{21}/\epsilon_{23} \simeq (P_{0+} + P_-)/(P_+ + P_-),$$
$$R_{234} = \epsilon_{43}/\epsilon_{23} \simeq (P_+ + P_{0-})/(P_+ + P_-), \quad (3)$$
$$R_{1234} = \epsilon_{41}/\epsilon_{23} \simeq (P_{0+} + P_{0-})/(P_+ + P_-),$$

were computed for all runs (all four run periods) when the polarimeter arms were located at the proper angles to detect

TABLE III. Mean values of the ratios R_{123}, R_{234}, and R_{1234} computed from the data in the four run periods, the associated χ^2 and the number of degrees of freedom. These ratios are described in Eq. (3).

	Ratio	χ^2	N_{DF}	χ^2/N_{DF}
R_{123}	0.5358 ± 0.0021	318.23	282	1.128
R_{234}	0.5361 ± 0.0025	209.56	216	0.970
R_{1234}	0.0617 ± 0.0031	234.89	216	1.087

pp elastic-scattering events, except the 800 MeV runs which had large asymmetries due to the large analyzing power A. Both carbon and CH_2 polarimeter target data from different runs were included. The weighted averages and χ^2/N_{DF} values are given in Table III. It can be seen that all three ratios are nearly constant, independent of beam energy. Also, R_{1234} is small and is reasonably consistent with $[R_{123}+R_{234}-1.0 = (0.072 \pm 0.0033)]$, as expected from Eq. (3).

In addition, the ratios of sums of polarizations, $R_{123} = R_{234} = R$ within statistical errors, or

$$P_{0+} + P_{-} = P_{+} + P_{0-}. \tag{4}$$

On the basis of this analysis and the results in Table III, R will be taken to be a constant ($R = 0.536 \pm 0.002$), and from Eq. (3),

$$\begin{aligned} P_{0+} &= R \cdot P_{+} + (R-1) \cdot P_{-}, \\ P_{0-} &= R \cdot P_{-} + (R-1) \cdot P_{+}. \end{aligned} \tag{5}$$

The constancy of the three ratios in Eqs. (3) can be achieved for a variety of accelerator and polarized ion source conditions if the ratios of the four beam polarizations $(P_1 : P_2 : P_3 : P_4) = (P_{0+} : P_{-} : P_{+} : P_{0-})$ were always fixed. The four polarizations would be multiplied by a different constant at different times as the ion source polarization varied or the accelerator depolarization changed. Also, Eqs. (5) indicate that if both P_{+} and P_{-} are multiplied by a constant, then P_{0+} and P_{0-} will also be multiplied by the same constant in order to keep R_{123} and R_{234} fixed. Although the data are *consistent* with the ratio of the four beam polarizations being constant, there are other possibilities. These other possibilities have a changing ratio P_{-}/P_{+} with P_{0+} and P_{0-} satisfying Eqs. (5),

$$P_{0+} : P_{-} : P_{+} : P_{0-} = \left[R + (R-1) \cdot \frac{P_{-}}{P_{+}} \right] : \frac{P_{-}}{P_{+}} : 1.0 : \left[(R-1) + R \cdot \frac{P_{-}}{P_{+}} \right],$$

or the four polarizations would need to satisfy conditions that are less likely physically. Thus the ratio of the four beam polarizations will be assumed to be constant.

Finally, the ratio of the P_3 (or P_2, etc.) polarization at two different time periods will be given by the corresponding ratio of ϵ_{23} values if the polarimeter and beam conditions remain unchanged. This follows from the assumption of constant ratios of the four beam polarizations at each energy. Usually these two periods were close in time, so the assumption of fixed beam conditions is reasonable. (However, in some cases during run period I, changes may have occurred.) Corrections to the data were applied in the Saclay analysis when the ratio of ϵ_{23} values indicated somewhat different average beam polarizations for the two target polarization periods, in an attempt to reduce systematic errors in the data from such changes.

The information from the measurements reported in Ref. [15] (see Sec. II A) can be incorporated with the results above. These later measurements are expected to apply to the present experiments since it has been shown that the polarimeter ratios are consistent with being constant over a period of several years. As a result, the ratios are expected to obey the relations:

$$P_{0+} : P_{-} : P_{+} : P_{0-} = 0.072 : 1.000 : 1.000 : 0.072. \tag{6}$$

Recall the P_j are all expected to be positive or all to be negative due to the form of Eqs. (1). The 0.072 values in Eq. (6) are from Eqs. (5) and the adopted value of R, and are consistent with the data reported in Ref. [15]. The results for the spin observables are not very sensitive to the value of R. Note that it was possible to obtain individual beam polarizations in [15], but not in this experiment, since the unpolarized ion source added a fifth polarization state with a value known to be zero, or equivalently it allowed determination of ϵ_{Ω}.

C. Scattering data

The analysis of the scattering data occurred in three stages. The first stage searched for changes in efficiency of trigger counters, wire chambers, or neutron counters within runs at each energy that could not be detected from scaler data alone. If such changes were found, the counter, wire, or wire chamber plane information was subsequently eliminated for all runs, beam, and target polarization states for that data set. Alternately, all data from certain spills were removed when hardware problems prevented readout of some wire chamber planes or when a high voltage power supply tripped off for a short time. The second stage analyzed the data in the spills that passed the scaler cuts, and for the detector information passing the detector cuts. The wire chamber data were decoded, particle positions in chambers calculated, and kinematic quantities such as scattering angles and particle momenta were computed. Cuts on some of the kinematic quantities were applied, and the data were binned as a function of scattering angle. The third stage estimated the remaining backgrounds, extracted the number of elastic-scattering events for each beam and target state, and computed the spin observables as a function of angle. This is described in detail in Sec. III D.

The first pass through the scattering data occurred mainly in the Argonne analysis. A number of quantities related to detector efficiencies were plotted as a function of spill number or of polarization state. The fraction of events for each trigger hodoscope counter (SH_i, WH_i) and neutron counter were computed for each spill and displayed as a function of spill number. At times, a counter would exhibit a changing

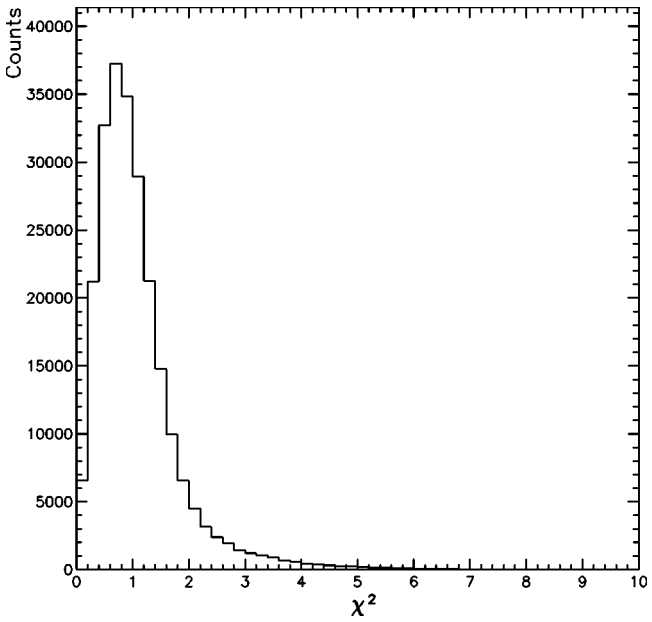

FIG. 4. χ-squared distribution for the fit to MWPC's C0, C1, and C2 in run period II.

fraction, such as $SH_5/\Sigma SH$. In addition, histograms of the number of times each hodoscope and neutron counter were hit were accumulated for events identified as pp-elastic scatters and also for all events recorded. These histograms were generated for each run, for each target polarization state, and for each beam polarization state. Changes in the fraction of events for each scintillation counter could be identified. In these cases, all events (both target and all four beam polarization states) having a signal in a counter with changing efficiency were eliminated from the next pass through the data in order to minimize systematic errors.

The MWPC data were also decoded in this stage. Histograms of the number of times each wire had a signal were made for each beam polarization state. These were compared to search for wires whose fraction changed outside statistical fluctuations. Typically a few wires were ''noisy'' in each MWPC plane, and often these wires were cut out because of their changing fractions. These isolated noisy wires were usually the only wires removed from the analysis.

Two-dimensional histograms of chamber positions were also generated. Some electronics problems were uncovered with the data in these plots. In addition, a region in chamber C1 was discovered that had a lower relative efficiency than the surrounding regions. It was a roughly circular region with diameter approximately 4 c.m. (from a previous experiment where the beam passed through this chamber). There was a concern that this region as a whole might be exhibiting changes in relative efficiency with time, especially during run periods III and IV. As a result, all events in this region were eliminated for all energies during those run periods, but not during the first two periods.

Finally, the relative efficiency for each MWPC plane was computed for each spill and plotted as a function of spill number. This relative efficiency was computed by finding the fraction of events with a signal on at least one wire in the plane. One hardware problem in run period II caused the relative efficiency to oscillate with time in a few planes. This problem was traced to missing information in the chamber plane identification code in the raw data. Fortunately, this problem occurred for only a couple of energies, and some of the data could be recovered. Another condition was also found where the MWPC relative efficiencies dropped to zero

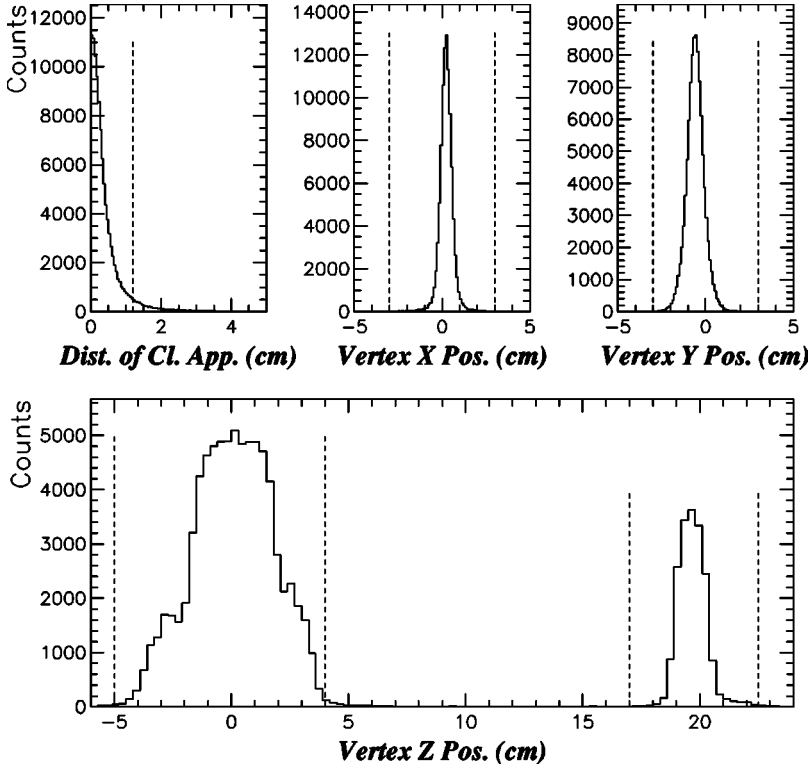

FIG. 5. Distributions of the distance of closest approach and of the vertex x,y,z positions, with all units in cm. The dashed lines indicate the typical positions of cuts; the cuts near $z \sim 19$ cm correspond to the CH_2 target.

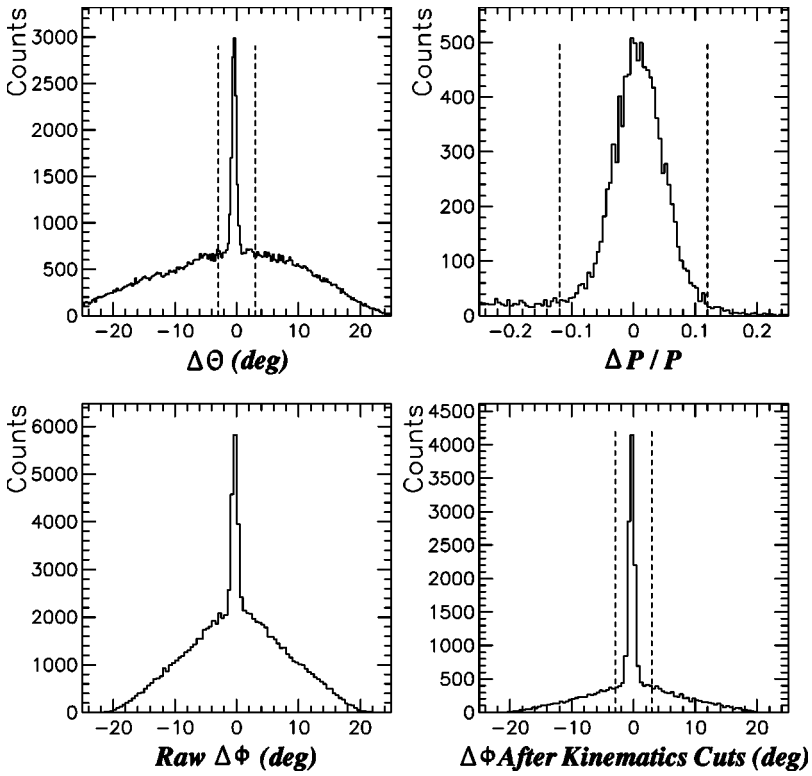

FIG. 6. Distributions of scattering angle difference ($\Delta\theta$ in degrees) and fractional momentum difference ($\Delta P/P$). The dashed lines indicate typical cuts applied. Also shown are the coplanarity, $\Delta\phi=\phi_L+\phi_R-180°$, distributions before and after kinematics cuts, where ϕ is the azimuthal angle of the detected outgoing particles.

in some spills, but beam was present and the scalers were not gated off. This condition could result in improper beam normalizations and false asymmetries in the data. Such spills were cut out of the analysis, in addition to those removed by the scaler cuts. Finally, problems with the wire chamber gas were observed in the relative efficiency plots before this was discovered on-line. As a result, data from sizeable regions of some planes, or whole wire planes at times, needed to be removed from the analysis at a few energies.

The second stage dealing with the scattering data was nearly identical for the two separate analyses. First, the events corresponding to spills that failed scaler cuts or that were determined to be bad from the preceeding pass were removed. The beam intensity monitor and polarization scaler values corresponding to those spills were not added to the sums for the run.

The scintillation counter hodoscope and neutron counter array data were processed next. Events were rejected if they did not have a unique counter in both the WH and SH hodoscopes, except for some early data in run period I. In the Argonne analysis, a weak cut on the correlation of the WH and SH counters was made to eliminate events that would clearly fail the elastic-scattering cuts. This was done to reduce the computer processing time. In the Saclay analysis, cuts were applied to the recorded timing information for the SH and neutron counters from $TD1$, and for the WH counters from $TG1$ and $TG2$. These cuts also eliminated some of the nonelastic events.

The analysis of the MWPC information followed. Raw data words were ignored that corresponded to individual wires or wire planes that had been identified as bad in the previous stage of the analysis. The remaining wire chamber data were converted to spatial positions. The coordinates of the ''hits'' in the chambers were processed by tracking software, unless there was too little information to define a track, in which case the event was rejected. Thus, at least two of

TABLE IV. Cross checks of the four relations $\mathcal{R}_j=1$ from Eqs. (8a)–(8c),(9) among the normalized elastic-scattering yields. The values of $\mathcal{R}_j$ are averages over all angles at each energy.

Energy (MeV)	$\mathcal{R}_1$	$\mathcal{R}_2$	$\mathcal{R}_3$	$\mathcal{R}_4$
1795	0.9901±0.0062	1.0003±0.0078	1.0011±0.0020	0.9738±0.0113
1845	1.0050±0.0076	1.0062±0.0067	0.9985±0.0020	0.9997±0.0124
1935			1.0031±0.0008	0.9834±0.0056
1955			1.0010±0.0010	0.9750±0.0056
1975			1.0027±0.0009	0.9876±0.0053
2035 II	1.0023±0.0076	1.0014±0.0083	1.0018±0.0022	0.9822±0.0132
2095 II	1.0087±0.0067	0.9893±0.0082	1.0011±0.0020	1.0171±0.0130

the three planes had to have good hits in chambers C3, C11, and C12, and sufficient information had to be available in C0, C1, and C2 to define a line. Furthermore, data from three or four planes within C0, or three planes within each of the other chambers, had to be consistent to some tolerance set by the software.

The tracking software first fit a straight line through the points in chambers C1 and C2 for run period I, and in C0, C1, and C2 for run period II. All combinations of multiple hits in each chamber plane were considered, and the fitted line with the minimum χ^2 was chosen; see Fig. 4. The line was then projected to chamber C3, located behind the Goupillon bending magnet, and compared to the observed hits. A coarse cut on the difference between the measured and predicted C3 positions was made. The momentum of the track was then computed. Finally, a straight line was fit to the hits in chambers C11 and C12.

The fitted lines from the two arms were projected to the target region to obtain the points at the distance of closest approach. The midpoint of the line segment connecting the two points was assigned to be the interaction point. Cuts were applied to the three coordinates of the interaction point and the distance of closest approach, as shown in Fig. 5. The polarized and the small unpolarized targets are clearly visible in the z distribution.

The angles from the two fitted lines were corrected for the polarized target magnetic field (θ_L for the polarimeter arm and θ_R for the magnetic spectrometer arm). The difference Δp of the measured momentum in the magnetic spectrometer and the value expected for elastic scattering from θ_R was computed and a cut applied. Similarly, the difference $\Delta\theta$ between the measured θ_R and the expected value from θ_L assuming elastic scattering was calculated and a cut also made. These two differences and typical cuts are shown in Fig. 6. The c.m. angle for each event was computed from the corrected laboratory angle in the magnetic spectrometer arm, θ_R.

The coplanarity ($\Delta\phi=\phi_L+\phi_R-180°$) was also calculated; see Fig. 6. For the Saclay analysis, counts from two separate regions in the coplanarity distribution were determined for each c.m. angle. One region included counts from the elastic-scattering peak plus background, whereas the other region was from the ''wings'' of the coplanarity distribution. The number of elastic-scattering events was then estimated from the difference of these counts. For the Argonne analysis, the background shape summed over all c.m. angles was estimated from the sum of two Gaussians fit to the coplanarity distribution in the wings, away from the peak ($|\Delta\phi|\sim 3-15°$). A fit with a single Gaussian was found to be inadequate. The coplanarity distributions were then recorded for each c.m. angle, and the background shape was normalized to the counts in the wings at each angle. Finally, the number of elastic events was determined in the elastic peak after subtraction of the background. The number of events surviving all cuts was similar for the two analyses, except for cases where a particular counter, wire, or wire chamber plane was removed from the Argonne analysis. The full reconstruction efficiency for the accepted elastic events was about 7% of the triggers at 2.0 GeV, and dropped with increasing energy down to 2.6% at 2.8 GeV.

D. Determination of the spin observable $A_{oono}=A_{ooon}$

The observed numbers of elastic-scattering events for a particular beam energy and c.m. angle were normalized to the relative beam intensity, AV, for each state to give n_{ij}. The subscript i corresponds to the target polarization state, and j to the beam polarization state. The normalized counts are expected to obey the following relations:

$$
\begin{aligned}
n_{+0+} &= C_0 N[1+P_{0+}A_{oono}+P_{T+}A_{ooon}+P_{0+}P_{T+}A_{oonn}],\\
n_{+-} &= C_0 N[1-P_{-}A_{oono}+P_{T+}A_{ooon}-P_{-}P_{T+}A_{oonn}],\\
n_{++} &= C_0 N[1+P_{+}A_{oono}+P_{T+}A_{ooon}+P_{+}P_{T+}A_{oonn}],\\
n_{+0-} &= C_0 N[1-P_{0-}A_{oono}+P_{T+}A_{ooon}-P_{0-}P_{T+}A_{oonn}],\\
n_{-0+} &= N[1+P_{0+}A_{oono}-P_{T-}A_{ooon}-P_{0+}P_{T-}A_{oonn}],\\
n_{--} &= N[1-P_{-}A_{oono}-P_{T-}A_{ooon}+P_{-}P_{T-}A_{oonn}],\\
n_{-+} &= N[1+P_{+}A_{oono}-P_{T-}A_{ooon}-P_{+}P_{T-}A_{oonn}],\\
n_{-0-} &= N[1-P_{0-}A_{oono}-P_{T-}A_{ooon}+P_{0-}P_{T-}A_{oonn}].
\end{aligned}
\tag{7}
$$

These equations are written so that all quantities P_j and P_{Ti} for the beam and target polarizations are expected to be positive values. The normalization N contains the cross section, solid angle, target length, efficiencies for AV and the spectrometer detectors, etc. It is assumed that the efficiencies change slowly compared to beam polarization state changes, or time scales of order seconds. However, the parameter C_0 allows for efficiency changes between target polarization state changes, or typically time scales of hours.

In Eqs. (7), the measured quantities include the eight yields, n_{ij}, and the two target polarizations, P_{T+} and P_{T-}. The unknown quantities include C_0, N, A_{oono}, A_{ooon}, A_{oonn}, and the four beam polarizations (P_{0+}, P_-, P_+, P_{0-}). The beam and target polarizations are independent of c.m. angle, while all other variables are angle dependent. In order to reduce the number of unknowns, the relationship in Eq. (6) will be assumed to hold; see Sec. III B. Therefore, only the magnitude $P_B=P_+=P_-$ must be determined.

The system of equations above, Eqs. (7), is neither linear nor independent. In fact, it can be shown that the normalized counts n_{ij} are connected by four independent relations, which can be expressed as ratios $\mathcal{R}_k$:

$$\mathcal{R}_1=\frac{n_{+0+}+n_{+0-}}{n_{++}+n_{+-}}=1, \tag{8a}$$

$$\mathcal{R}_2=\frac{n_{-0+}+n_{-0-}}{n_{-+}+n_{--}}=1, \tag{8b}$$

$$\mathcal{R}_3=\frac{n_{+0+}n_{--}+n_{+-}n_{-+}+n_{++}n_{-0+}}{n_{+-}n_{-0+}+n_{++}n_{--}+n_{+0+}n_{-+}}=1, \tag{8c}$$

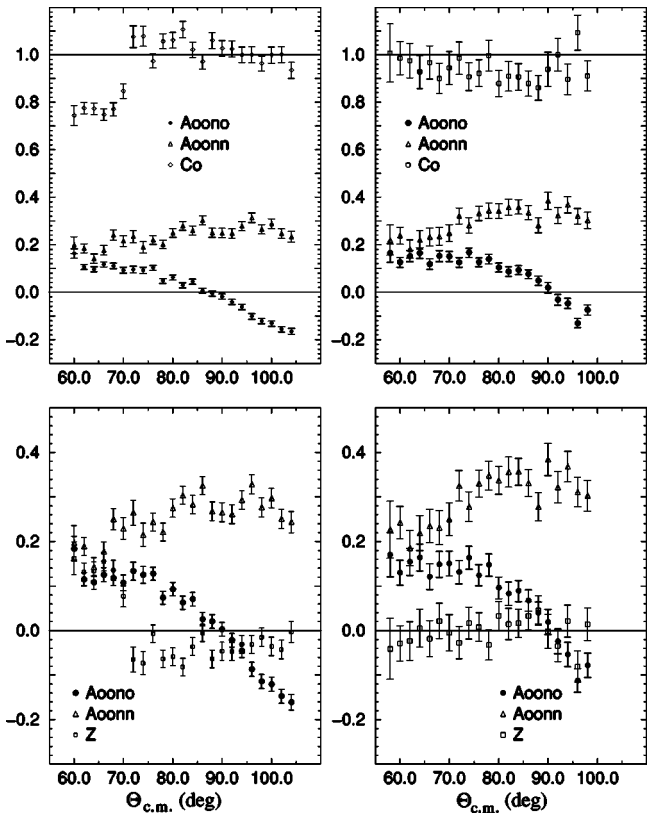

FIG. 7. Plots of the spin observables A_{oon} and A_{oonn} as functions of $\theta_{\text{c.m.}}$. The upper two plots are for the second method of analysis, described in the text, and the lower two plots are for the same runs with the first method. A large change in the relative normalization, C_0, is observed for the left data (2225 MeV, run period IV), leading to considerable differences in $Z=A_{oono}-A_{ooon}$. This behavior was traced to a problem with the MWPC gas. The runs on the right (2225 MeV, run period I) show no such problems.

$$\mathcal{R}_4=\frac{P_{0+}n_{+-}n_{-+}+P_{-}n_{+0+}n_{-+}+P_{+}n_{+0+}n_{--}}{P_{0+}n_{++}n_{--}+P_{-}n_{++}n_{-0+}+P_{+}n_{+-}n_{-0+}}=1. \tag{8d}$$

The relations for $\mathcal{R}_1$ and $\mathcal{R}_2$ follow from Eqs. (4) and (7), and are a consequence of the operation of the polarized ion source. The results in Eqs. (8c) and (8d) for $\mathcal{R}_3$ and $\mathcal{R}_4$ are completely general, and involve only three of the four beam polarization states (here P_+, P_-, and P_{0+}). Similar equations could be written in terms of a different set of three polarizations, for example omitting P_{0+} instead of P_{0-}. For this experiment, Eqs. (5) and (6) can be used to rewrite Eq. (8d) as

$$\mathcal{R}_4=\frac{(2R-1)n_{+-}n_{-+}+n_{+0+}n_{-+}+n_{+0+}n_{--}}{(2R-1)n_{++}n_{--}+n_{++}n_{-0+}+n_{+-}n_{-0+}}=1. \tag{9}$$

There were only two beam polarization states for most of run period I, so the $\mathcal{R}_k$ could not be evaluated. The values of $\mathcal{R}_1-\mathcal{R}_4$ for run period II, and of $\mathcal{R}_3$ and $\mathcal{R}_4$ for the few energies with three beam polarization states in run period I are given in Table IV. These values are all consistent with 1.0, as expected, and they provide a limit on the size of certain systematic errors. The value of $\mathcal{R}_4$ computed from Eq. (9) and given in Table IV tests not only the consistency of the data, but also is a check on Eqs. (5) and (6). Note each entry in Table IV is an average over all c.m. angles at that energy. There is a similar table in the accompanying paper (Ref. [2]), and again the four ratios $\mathcal{R}_k$ are consistent with 1.0.

Two methods were used to derive the physics parameters as functions of c.m. angle. The existence of the four relations in Eqs. (8) among the eight measured yields n_{ij} in Eqs. (7) allows only four unknowns to be determined at each angle. However, there are six quantities remaining, namely P_B, C_0, N, A_{ooon}, A_{oono}, and A_{oonn}. Thus, additional constraints must be applied.

In one method, C_0 was assumed to be independent of c.m. angle, similar to P_B. This would be true if all detector efficiencies were constant, except perhaps for the AV counters that normalized the beam intensity, or the $TD1$ or $TG1$ counters that were part of the experimental trigger. The Saclay analysis used this approach, varying C_0 and P_B until $A_{ooon}=A_{oono}$ within errors over the whole angular range. Six relations were considered: the four for $n_{+-},n_{++},n_{--},n_{-+}$ in Eqs. (7), and

$$\begin{aligned} n_{+0+}+n_{+0-}&=C_0N[2+(P_{0+}-P_{0-})A_{oono}+2P_{T+}A_{ooon}\\ &\quad+(P_{0+}-P_{0-})P_{T+}A_{oonn}]\\ &=2C_0N[1+P_{T+}A_{ooon}], \end{aligned}$$

$$\begin{aligned} n_{-0+}+n_{-0-}&=N[2+(P_{0+}-P_{0-})A_{oono}-2P_{T-}A_{ooon}\\ &\quad-(P_{0+}-P_{0-})P_{T-}A_{oonn}]\\ &=2N[1-P_{T-}A_{ooon}]. \end{aligned}$$

At most energies C_0 was close to or identically equal to 1.00. As noted in Sec. III B, different beam polarizations were used for n_{+-},n_{++} and for n_{--},n_{-+} at six energies (1955, 2015, 2035 I, 2075, 2135, and 2155 MeV–2035 I is from run period I). The ratio of beam polarizations during the two target polarization periods at each energy was set equal to the corresponding ratio of ϵ_{23} values from the SD3 polarimeter; see Eq. (2a). The final A_{oon} values from the Saclay analysis were approximately the average, $(A_{ooon}+A_{oono})/2$, at each angle.

In the second method, it was assumed that $A_{ooon}=A_{oono}$ for each angle, but C_0 was left to vary with angle. Any points where C_0 changed outside errors would signal an angle dependent efficiency change. This method was the first step in the Argonne analysis. A value of P_B was assumed, and the values of C_0, A_N, and A_{oonn} were determined at each angle by a χ^2 procedure using all eight relations in Eqs. (7). The beam polarization was then found by minimizing the sum of the χ^2 values at each angle. Figure 7 shows the results at one energy and two run periods, one with a constant C_0 and the other with a varying C_0. In many cases, the cause of the change in C_0 was identified with a particular

TABLE V. (a) Measured values of the analyzing power $A_{oon}=A_N$ at $T=1795$ MeV. The quantities $\langle\theta_{\text{c.m.}}\rangle$ and $-t$ are the central values of the c.m. angle and four-momentum transfer squared for each bin in degrees and $(\text{GeV}/c)^2$, respectively. The relative and additive systematic errors are ± 0.106 and ± 0.003, respectively. (b) Measured values of $A_{oon}=A_N$ at 1845 MeV. The relative and additive systematic errors are ± 0.068 and ± 0.001. (c) Measured values of $A_{oon}=A_N$ at 1935 MeV. The relative and additive systematic errors are ± 0.091 and ± 0.003. (d) Measured values of $A_{oon}=A_N$ at 1955 MeV. The relative and additive systematic errors are ± 0.082 and ± 0.003. (e) Measured values of $A_{oon}=A_N$ at 1975 MeV. The relative and additive systematic errors are ± 0.067 and ± 0.002. (f) Measured values of $A_{oon}=A_N$ at 1995 MeV. The relative and additive systematic errors are ± 0.098 and ± 0.002. (g) Measured values of $A_{oon}=A_N$ at 2015 MeV. The relative and additive systematic errors are ± 0.075 and ± 0.002. (h) Measured values of $A_{oon}=A_N$ at 2035 MeV during run period I. The relative and additive systematic errors are ± 0.065 and ± 0.003. (i) Measured values of $A_{oon}=A_N$ at 2035 MeV during run period II. The relative and additive systematic errors are ± 0.059 and ± 0.002. (j) Measured values of $A_{oon}=A_N$ at 2055 MeV. The relative and additive systematic errors are ± 0.065 and ± 0.003. (k) Measured values of $A_{oon}=A_N$ at 2075 MeV. The relative and additive systematic errors are ± 0.058 and ± 0.003. (l) Measured values of $A_{oon}=A_N$ at 2095 MeV during run period I. The relative and additive systematic errors are ± 0.062 and ± 0.003. (m) Measured values of $A_{oon}=A_N$ at 2095 MeV during run period II. The relative and additive systematic errors are ± 0.043 and ± 0.002. (n) Measured values of $A_{oon}=A_N$ at 2115 MeV. The relative and additive systematic errors are ± 0.066 and ± 0.003. (o) Measured values of $A_{oon}=A_N$ at 2135 MeV. The relative and additive systematic errors are ± 0.065 and ± 0.003. (p) Measured values of $A_{oon}=A_N$ at 2155 MeV. The relative and additive systematic errors are ± 0.062 and ± 0.004. (q) Measured values of $A_{oon}=A_N$ at 2175 MeV. The relative and additive systematic errors are ± 0.062 and ± 0.003. (r) Measured values of $A_{oon}=A_N$ at 2205 MeV. The relative and additive systematic errors are ± 0.068 and ± 0.003. (s) Measured values of $A_{oon}=A_N$ at 2215 MeV. The relative and additive systematic errors are ± 0.081 and ± 0.003. (t) Measured values of $A_{oon}=A_N$ at 2225 MeV. The relative and additive systematic errors are ± 0.065 and ± 0.003. (u) Measured values of $A_{oon}=A_N$ at 2235 MeV. The relative and additive systematic errors are ± 0.060 and ± 0.004.

$\langle\theta_{\text{c.m.}}\rangle$	$-t$	A_{oon}	ΔA_{oon}
	(a) 1795 MeV		
60.0	0.842	0.044	0.016
62.0	0.894	0.089	0.016
64.0	0.946	0.056	0.017
66.0	0.999	0.061	0.016
68.0	1.053	0.042	0.016
70.0	1.108	0.075	0.016
72.0	1.164	0.082	0.017
74.0	1.220	0.047	0.016
76.0	1.277	0.040	0.017
78.0	1.334	0.021	0.017
80.0	1.392	0.039	0.017
82.0	1.450	0.002	0.016
84.0	1.508	0.011	0.016
86.0	1.567	0.028	0.016
88.0	1.625	0.021	0.017
90.0	1.684	−0.044	0.018
92.0	1.743	−0.058	0.017
94.0	1.802	−0.036	0.016
	(b) 1845 MeV		
56.0	0.763	0.147	0.025
58.0	0.814	0.140	0.012
60.0	0.866	0.106	0.012
62.0	0.918	0.118	0.012
64.0	0.972	0.065	0.013
66.0	1.027	0.049	0.013
68.0	1.083	0.059	0.012
70.0	1.139	0.077	0.012
72.0	1.196	0.057	0.013
74.0	1.254	0.073	0.012
76.0	1.312	0.084	0.013
78.0	1.371	0.037	0.014
80.0	1.431	0.054	0.013
82.0	1.490	0.039	0.013
84.0	1.550	0.032	0.013
86.0	1.610	0.021	0.013
88.0	1.671	0.000	0.014
90.0	1.731	−0.032	0.014
92.0	1.792	−0.014	0.014
94.0	1.852	−0.005	0.014
96.0	1.912	−0.024	0.014
98.0	1.972	−0.020	0.014
100.0	2.032	−0.049	0.021
	(c) 1935 MeV		
56.5	0.815	0.144	0.027
58.1	0.856	0.094	0.015
59.9	0.906	0.104	0.025
62.0	0.964	0.098	0.022
64.0	1.019	0.116	0.016
66.0	1.077	0.090	0.028
68.0	1.136	0.096	0.021
70.0	1.194	0.092	0.029
72.0	1.254	0.102	0.018
74.0	1.315	0.091	0.017
76.0	1.377	0.094	0.017
78.0	1.437	0.123	0.026
80.1	1.502	0.103	0.018
82.0	1.563	0.100	0.032
84.0	1.627	0.065	0.025
86.0	1.688	0.018	0.021
88.0	1.751	0.057	0.029
90.0	1.815	0.035	0.018
92.0	1.880	0.001	0.037
94.0	1.942	0.005	0.021
95.9	2.003	−0.012	0.024
97.3	2.047	−0.047	0.050
	(d) 1955 MeV		
60.0	0.916	0.080	0.018
62.0	0.973	0.094	0.029
64.0	1.030	0.064	0.027

TABLE V. (*Continued.*)

$\langle\theta_{\text{c.m.}}\rangle$	$-t$	A_{oon}	ΔA_{oon}	$\langle\theta_{\text{c.m.}}\rangle$	$-t$	A_{oon}	ΔA_{oon}
65.9	1.087	0.081	0.017	88.0	1.807	0.050	0.023
68.0	1.148	0.081	0.022	90.0	1.872	0.004	0.024
70.0	1.207	0.134	0.019	92.0	1.937	−0.020	0.024
72.0	1.267	0.109	0.018	94.0	2.002	−0.059	0.023
74.0	1.329	0.091	0.020	96.0	2.068	−0.071	0.023
76.0	1.391	0.046	0.019	98.0	2.132	−0.107	0.044
78.0	1.453	0.047	0.029	(g) 2015 MeV			
80.0	1.517	0.045	0.025	56.7	0.853	0.090	0.048
82.0	1.580	0.008	0.026	58.1	0.891	0.124	0.018
84.0	1.643	0.038	0.021	60.0	0.946	0.132	0.017
86.0	1.706	0.025	0.026	62.0	1.003	0.153	0.016
88.0	1.770	0.007	0.018	64.0	1.062	0.138	0.017
90.0	1.834	−0.030	0.031	65.9	1.120	0.150	0.020
92.0	1.900	−0.046	0.033	68.0	1.184	0.137	0.017
94.0	1.962	−0.070	0.022	70.0	1.243	0.108	0.018
95.9	2.024	−0.092	0.025	72.0	1.307	0.094	0.019
(e) 1975 MeV				74.0	1.369	0.110	0.029
56.7	0.836	0.191	0.038	76.0	1.434	0.124	0.021
58.1	0.874	0.115	0.013	78.0	1.497	0.101	0.018
60.0	0.925	0.108	0.017	80.0	1.564	0.078	0.019
62.0	0.983	0.112	0.013	82.0	1.627	0.098	0.030
64.0	1.041	0.086	0.019	84.0	1.693	0.061	0.019
65.9	1.098	0.110	0.016	86.0	1.758	0.034	0.029
68.0	1.160	0.113	0.018	88.0	1.824	0.045	0.027
70.0	1.219	0.099	0.016	90.0	1.890	−0.003	0.027
72.0	1.281	0.106	0.017	92.1	1.960	−0.015	0.022
74.0	1.342	0.096	0.016	94.0	2.022	−0.012	0.024
76.0	1.405	0.109	0.018	96.0	2.088	−0.049	0.027
78.0	1.468	0.090	0.015	97.4	2.136	−0.097	0.041
80.1	1.533	0.047	0.015	(h) 2035 MeV			
82.0	1.595	0.082	0.015	56.7	0.862	0.181	0.087
84.0	1.660	0.059	0.015	58.1	0.900	0.153	0.017
86.0	1.723	0.016	0.014	60.0	0.955	0.138	0.015
88.0	1.788	0.017	0.015	62.0	1.013	0.133	0.015
90.0	1.853	−0.020	0.017	64.0	1.072	0.136	0.017
92.0	1.919	0.001	0.020	65.9	1.130	0.117	0.022
94.0	1.983	−0.053	0.017	68.0	1.194	0.149	0.017
96.0	2.046	−0.039	0.015	70.0	1.256	0.138	0.015
97.4	2.092	−0.098	0.030	72.0	1.319	0.169	0.024
(f) 1995 MeV				74.0	1.383	0.110	0.018
62.0	0.993	0.119	0.021	76.0	1.447	0.131	0.016
64.0	1.051	0.117	0.021	78.0	1.512	0.093	0.017
66.0	1.111	0.106	0.022	80.0	1.578	0.052	0.043
68.0	1.171	0.117	0.023	82.0	1.644	0.089	0.022
70.0	1.232	0.093	0.022	84.0	1.710	0.048	0.041
72.0	1.293	0.100	0.023	86.0	1.776	0.045	0.021
74.0	1.356	0.103	0.022	88.0	1.843	0.078	0.029
76.0	1.419	0.086	0.023	90.0	1.909	−0.002	0.018
78.0	1.483	0.052	0.022	92.1	1.979	0.010	0.024
80.0	1.547	0.094	0.022	94.0	2.042	−0.007	0.018
82.0	1.611	0.089	0.022	96.0	2.109	−0.055	0.017
84.0	1.676	0.071	0.022	97.5	2.159	−0.072	0.026
86.0	1.741	0.065	0.023				

TABLE V. (*Continued.*)

$\langle\theta_{\text{c.m.}}\rangle$	$-t$	A_{oon}	ΔA_{oon}
	(i) 2035 MeV		
60.1	0.959	0.131	0.016
62.0	1.013	0.105	0.025
64.0	1.072	0.125	0.015
65.9	1.130	0.131	0.014
68.1	1.197	0.149	0.018
70.0	1.256	0.140	0.013
72.0	1.319	0.135	0.016
74.0	1.383	0.121	0.015
76.0	1.447	0.112	0.013
78.0	1.512	0.093	0.017
80.0	1.578	0.086	0.015
82.1	1.647	0.056	0.013
84.0	1.710	0.075	0.020
86.0	1.776	0.010	0.013
88.0	1.843	0.022	0.014
90.0	1.909	−0.034	0.015
92.0	1.976	−0.014	0.016
94.0	2.042	−0.035	0.016
96.0	2.109	−0.078	0.017
97.9	2.173	−0.068	0.016
99.8	2.234	−0.086	0.022
101.3	2.283	−0.088	0.055
	(j) 2055 MeV		
56.7	0.871	0.103	0.085
58.1	0.908	0.136	0.022
60.0	0.965	0.134	0.017
62.0	1.023	0.116	0.016
64.0	1.083	0.130	0.017
65.9	1.141	0.143	0.022
68.1	1.208	0.129	0.018
70.0	1.268	0.128	0.017
72.0	1.334	0.108	0.017
74.0	1.397	0.112	0.019
76.0	1.462	0.132	0.017
78.0	1.527	0.141	0.021
80.0	1.594	0.107	0.017
82.0	1.659	0.082	0.022
84.0	1.726	0.071	0.016
86.0	1.793	0.032	0.019
88.0	1.861	0.027	0.020
90.0	1.928	0.018	0.019
92.1	1.997	−0.015	0.019
94.0	2.063	−0.027	0.020
96.0	2.129	−0.053	0.019
97.6	2.183	−0.115	0.047
	(k) 2075 MeV		
58.1	0.919	0.159	0.015
60.0	0.974	0.121	0.013
62.0	1.033	0.146	0.015
64.0	1.093	0.130	0.013
65.9	1.153	0.134	0.014
68.0	1.219	0.139	0.015
70.0	1.280	0.122	0.015
72.0	1.347	0.117	0.022
74.0	1.409	0.099	0.015
76.0	1.476	0.108	0.015
78.0	1.543	0.129	0.015
80.0	1.608	0.059	0.019
82.0	1.676	0.034	0.016
84.0	1.743	0.048	0.016
86.0	1.811	0.019	0.018
88.0	1.879	0.020	0.017
90.0	1.946	−0.009	0.016
92.0	2.016	−0.043	0.024
94.0	2.082	−0.032	0.017
96.0	2.151	−0.066	0.019
97.7	2.207	−0.110	0.022
	(l) 2095 MeV		
58.1	0.928	0.169	0.020
60.0	0.984	0.134	0.022
62.0	1.043	0.152	0.015
65.0	1.135	0.144	0.012
68.0	1.231	0.137	0.016
70.0	1.293	0.162	0.025
72.0	1.358	0.124	0.026
74.0	1.424	0.125	0.023
76.0	1.490	0.107	0.017
78.0	1.557	0.126	0.027
80.0	1.624	0.056	0.028
82.0	1.692	0.085	0.022
84.0	1.760	0.071	0.026
86.0	1.829	0.040	0.021
88.0	1.897	−0.013	0.023
90.0	1.966	0.003	0.027
92.0	2.034	−0.027	0.023
94.0	2.103	−0.063	0.023
96.0	2.171	−0.059	0.021
97.6	2.227	−0.117	0.026
	(m) 2095 MeV		
58.7	0.945	0.125	0.066
60.1	0.985	0.118	0.014
62.0	1.043	0.127	0.014
64.0	1.104	0.128	0.014
65.9	1.164	0.139	0.013
68.1	1.232	0.154	0.013
70.0	1.293	0.135	0.014
72.0	1.358	0.133	0.017
74.0	1.424	0.142	0.015
75.5	1.473	0.113	0.014
78.0	1.557	0.118	0.014
79.5	1.607	0.069	0.015
82.0	1.692	0.072	0.017
84.0	1.760	0.061	0.014
86.0	1.829	0.049	0.013
88.0	1.897	0.007	0.014

TABLE V. (*Continued.*)

$\langle\theta_{\text{c.m.}}\rangle$	$-t$	A_{oon}	ΔA_{oon}	$\langle\theta_{\text{c.m.}}\rangle$	$-t$	A_{oon}	ΔA_{oon}
90.0	1.966	−0.032	0.014	60.1	1.013	0.163	0.016
92.0	2.034	−0.070	0.020	62.0	1.073	0.193	0.016
94.0	2.103	−0.087	0.016	64.0	1.136	0.162	0.015
96.0	2.171	−0.083	0.015	66.0	1.199	0.194	0.018
98.0	2.239	−0.111	0.015	68.0	1.265	0.196	0.018
100.4	2.322	−0.124	0.016	70.0	1.330	0.185	0.018
102.0	2.374	−0.145	0.022	72.0	1.397	0.170	0.017
	(n) 2115 MeV			74.0	1.465	0.152	0.019
58.3	0.942	0.327	0.021	76.0	1.533	0.154	0.017
60.1	0.995	0.156	0.016	78.0	1.602	0.138	0.017
62.0	1.052	0.113	0.019	79.9	1.668	0.132	0.018
64.0	1.115	0.118	0.018	82.0	1.742	0.075	0.018
66.0	1.176	0.131	0.017	84.0	1.810	0.084	0.019
68.0	1.243	0.157	0.021	86.0	1.881	0.067	0.018
70.0	1.306	0.124	0.019	88.0	1.951	0.033	0.018
72.1	1.374	0.129	0.027	90.0	2.021	0.014	0.020
74.0	1.437	0.136	0.020	92.0	2.092	−0.007	0.023
76.0	1.504	0.100	0.024	94.0	2.163	−0.060	0.020
78.0	1.572	0.099	0.019	96.0	2.233	−0.062	0.018
79.9	1.636	0.095	0.022	97.8	2.295	−0.045	0.022
82.0	1.709	0.074	0.018		(q) 2175 MeV		
84.0	1.777	0.055	0.020	58.4	0.972	0.140	0.030
86.0	1.847	0.034	0.024	60.1	1.022	0.146	0.016
88.0	1.914	0.007	0.019	62.0	1.083	0.180	0.015
90.0	1.983	−0.004	0.026	64.0	1.146	0.153	0.015
92.0	2.054	−0.024	0.023	66.0	1.211	0.195	0.019
94.0	2.123	−0.059	0.023	68.0	1.276	0.144	0.018
96.0	2.192	−0.083	0.020	70.0	1.343	0.144	0.017
97.7	2.251	−0.106	0.031	72.0	1.410	0.158	0.018
	(o) 2135 MeV			74.0	1.479	0.162	0.018
58.3	0.952	0.226	0.033	76.0	1.547	0.133	0.017
60.0	1.003	0.131	0.019	78.0	1.616	0.110	0.017
62.0	1.062	0.160	0.016	79.9	1.684	0.096	0.019
64.0	1.125	0.170	0.018	82.1	1.759	0.110	0.018
66.0	1.188	0.118	0.024	84.0	1.827	0.081	0.020
68.0	1.254	0.134	0.018	86.0	1.899	0.041	0.018
70.0	1.318	0.169	0.017	88.0	1.968	0.034	0.020
72.0	1.385	0.098	0.022	90.0	2.041	−0.004	0.020
74.0	1.451	0.130	0.018	92.0	2.111	−0.031	0.020
76.0	1.519	0.122	0.022	94.0	2.183	−0.054	0.020
78.0	1.587	0.112	0.020	96.0	2.254	−0.079	0.024
79.9	1.654	0.089	0.019	97.8	2.317	−0.107	0.026
82.0	1.725	0.078	0.018		(r) 2205 MeV		
84.0	1.794	0.031	0.019	58.5	0.988	0.144	0.048
86.0	1.864	0.053	0.024	60.0	1.036	0.160	0.026
88.0	1.932	0.002	0.024	62.0	1.098	0.171	0.025
90.0	2.002	−0.008	0.021	64.0	1.162	0.103	0.022
92.0	2.073	−0.031	0.023	66.0	1.228	0.166	0.021
94.0	2.143	−0.057	0.019	68.0	1.293	0.163	0.025
96.0	2.213	−0.062	0.021	70.0	1.360	0.133	0.035
97.8	2.274	−0.082	0.023	72.0	1.431	0.127	0.021
	(p) 2155 MeV			74.0	1.500	0.124	0.020
58.4	0.962	0.146	0.023	76.0	1.568	0.144	0.019

TABLE V. (*Continued.*)

$\langle\theta_{\text{c.m.}}\rangle$	$-t$	A_{oon}	ΔA_{oon}	$\langle\theta_{\text{c.m.}}\rangle$	$-t$	A_{oon}	ΔA_{oon}
78.0	1.639	0.104	0.021	66.0	1.239	0.154	0.019
80.0	1.709	0.090	0.022	67.9	1.303	0.177	0.024
82.1	1.783	0.087	0.027	70.0	1.374	0.177	0.019
84.0	1.852	0.064	0.022	72.0	1.444	0.176	0.020
86.0	1.925	−0.008	0.024	74.0	1.512	0.205	0.030
88.0	1.996	−0.002	0.033	76.0	1.583	0.147	0.018
90.0	2.069	−0.021	0.027	78.0	1.654	0.174	0.024
92.0	2.140	−0.034	0.025	80.0	1.725	0.102	0.019
94.0	2.214	−0.074	0.022	82.1	1.800	0.089	0.021
96.0	2.285	−0.071	0.022	84.0	1.869	0.102	0.019
97.8	2.349	−0.123	0.025	86.0	1.942	0.084	0.023
	(s) 2215 MeV			88.0	2.014	0.043	0.021
58.5	0.994	0.154	0.053	90.0	2.088	0.035	0.022
60.1	1.041	0.140	0.022	92.0	2.160	0.008	0.023
62.0	1.103	0.137	0.020	94.0	2.233	−0.050	0.021
64.0	1.167	0.141	0.023	96.0	2.306	−0.096	0.033
66.0	1.233	0.182	0.027	97.8	2.370	−0.093	0.027
68.0	1.299	0.152	0.037		(u) 2235 MeV		
70.0	1.367	0.188	0.036	60.1	1.050	0.193	0.032
72.0	1.436	0.150	0.028	62.0	1.113	0.216	0.028
74.0	1.505	0.112	0.021	64.0	1.178	0.209	0.021
76.0	1.575	0.119	0.020	66.0	1.244	0.211	0.039
78.0	1.646	0.076	0.025	67.9	1.310	0.174	0.022
80.0	1.717	0.091	0.026	70.0	1.380	0.187	0.026
82.1	1.793	0.095	0.048	72.0	1.449	0.180	0.021
84.0	1.861	0.023	0.023	74.0	1.520	0.157	0.026
86.0	1.934	0.007	0.032	76.0	1.590	0.182	0.032
88.0	2.006	0.025	0.024	78.0	1.661	0.189	0.026
90.0	2.078	−0.010	0.028	80.0	1.733	0.150	0.036
92.0	2.150	−0.078	0.026	82.1	1.809	0.092	0.023
94.1	2.226	−0.050	0.025	84.0	1.878	0.088	0.027
96.0	2.296	−0.112	0.035	86.0	1.951	0.104	0.021
97.8	2.359	−0.047	0.028	88.0	2.024	0.048	0.023
	(t) 2225 MeV			90.0	2.097	0.050	0.040
58.6	1.000	0.166	0.064	92.0	2.169	0.028	0.045
60.1	1.046	0.165	0.019	94.1	2.246	−0.063	0.039
62.0	1.108	0.187	0.019	96.0	2.316	−0.068	0.027
64.0	1.172	0.191	0.019	97.7	2.380	−0.066	0.047

detector element, such as a hodoscope counter or MWPC wires. The complete analysis was then repeated with a cut to remove the offending element. In the remaining cases, the angles with the different C_0 values were excluded.

The second step in the Argonne analysis occurred after the C_0 values for the remaining angles appeared to be constant. A procedure very similar to the Saclay analysis was used to determine A_{oon} and A_{oonn}, except that all eight relations in Eqs. (7) were used.

The Saclay and Argonne values for A_{oon} were then combined. The value of A_N was chosen to be the unweighted average of A_{oon} results at each angle, since these quantities are not statistically independent. The error was assigned to be the smaller statistical error in quadrature with half the difference between the two A_{oon} values. This procedure provides an estimate of the systematic errors associated with the different analysis methods and cuts. For most points, this estimated systematic error was smaller that the statistical uncertainty. The final values are given in Table V and Figs. 8–12.

E. Systematic errors

There are several types of systematic errors for this experiment. One type is associated with the knowledge of the absolute beam and target polarizations. This relative error is in common to all points at a particular energy and run period. It was computed from the estimated relative error on the

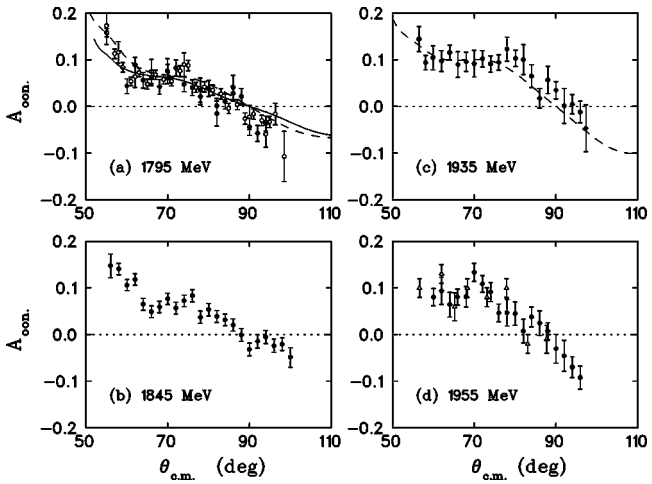

FIG. 8. Experimental results for $A_{oon}=A_N$ as a function of c.m. angle at 1795, 1845, 1935, and 1955 MeV. The points correspond to: solid circles—this experiment; open circles indicate Perrot *et al.* [18]; and open triangles indicate Albrow *et al.* [28]. The solid curve is a PSA prediction of the Saclay-Geneva group [36], and the dashed curves are from Arndt *et al.* [37].

target polarization ($\pm 3\%$) and the corresponding variation in A_{oon}, and is quoted in Table V. The systematic errors are larger than for the target polarization alone, because $A_{oon} \cong (A_{oono}+A_{ooon})/2$, and the results for A_{oono} require knowledge of the derived beam polarization. Furthermore, at 2035 II (run period II) and 2095 I MeV, the estimated relative errors were increased to compensate for the fact that the target polarization was not measured after the elastics data were collected for one target state; see Sec. II C.

A second type of systematic error is caused by the methods to estimate backgrounds under the elastic peak in Fig. 6. These are included in the quoted errors in Table V as a

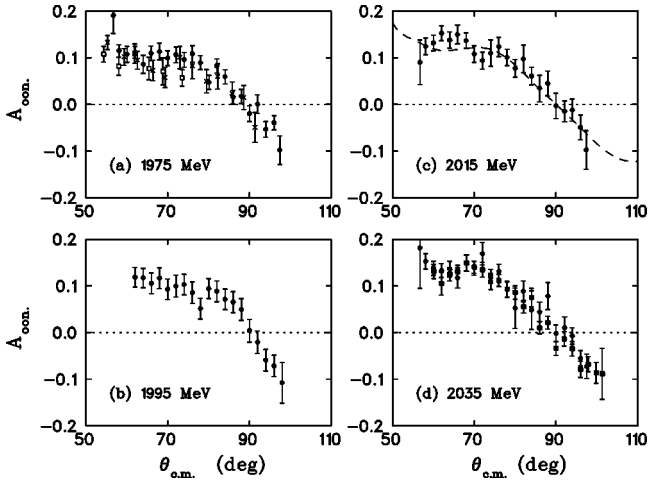

FIG. 9. Experimental results for $A_{oon}=A_N$ as a function of c.m. angle at 1975, 1995, 2015, and 2035 MeV. The values at 2035 MeV from run period I are shown as solid circles, and from run period II as solid squares. All other data from this paper are given as solid circles. The open squares are results from Parry *et al.* [30], and the crosses from Bell *et al.* [31]. The dashed curve is from a PSA prediction of Arndt *et al.* [37].

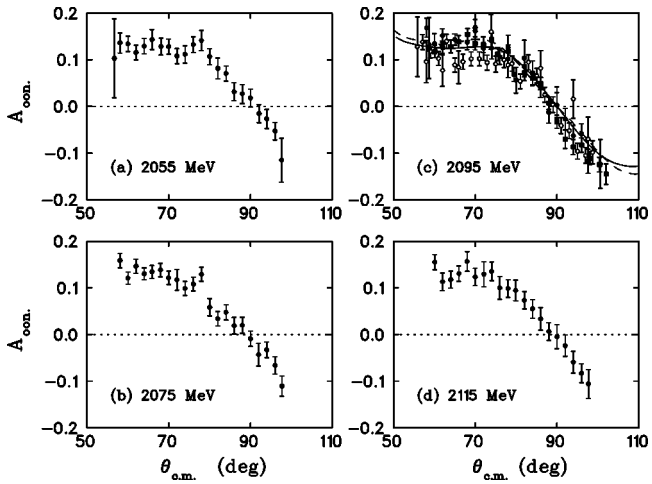

FIG. 10. Experimental results for $A_{oon}=A_N$ as a function of c.m. angle at 2055, 2075, 2095, and 2115 MeV. The values at 2095 MeV from run period I are shown as solid circles, and from run period II as solid squares. All other data from this paper are given as solid circles. The open circles are results from Perrot *et al.* [18]. The solid curve is a PSA prediction of the Saclay-Geneva group [36], and the dashed curve is from Arndt *et al.* [37].

contribution from the difference in A_{oon} results at each angle between the Saclay and Argonne analyses; see Sec. III D. Then the total error on A_{oon} is given by three contributions in quadrature: (a) the combined statistical error and estimate of systematic uncertainty for determining backgrounds, (b) the relative error times A_{oon} corresponding to uncertainties in the absolute beam and target polarizations, and (c) the additive systematic error due to the uncertainty in the value of C_0 in common to all points in a data set:

$$(\delta A_{oon})^2=(\delta A_{oon,stat})^2+(A_{oon}\times\sigma_{\rm rel})^2+(\sigma_{\rm add})^2.$$

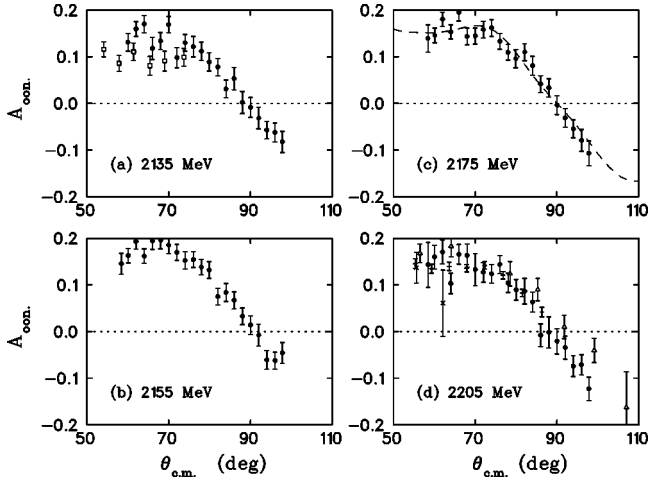

FIG. 11. Experimental results for $A_{oon}=A_N$ as a function of c.m. angle at 2135, 2155, 2175, and 2205 MeV. The points correspond to solid circles for this experiment; open squares indicate Parry *et al.* [30]; open triangles indicate Miller *et al.* [29]; crosses indicate Diebold *et al.* [33]; and pluses indicate Makdisi *et al.* [32]. The dashed curve is from a PSA prediction of Arndt *et al.* [37].

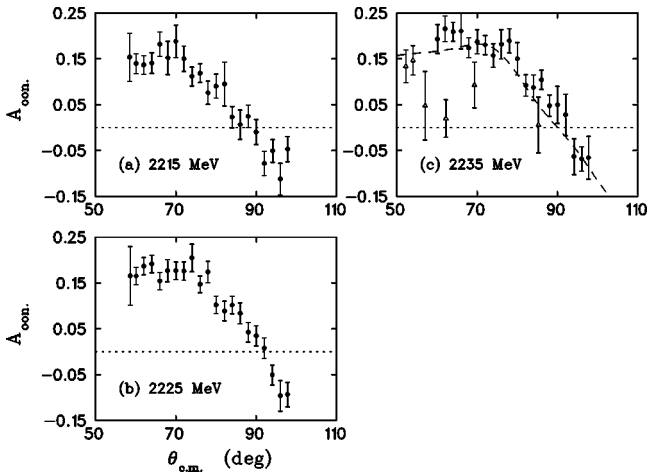

FIG. 12. Experimental results for $A_{oon}=A_N$ as a function of c.m. angle at 2215, 2225, and 2235 MeV. The solid circles correspond to this experiment and the open triangles to data from Neal and Longo [34]. The dashed curve is from a PSA prediction of Arndt *et al.* [37].

The relative and additive systematic errors ($\sigma_{\rm rel}$ and $\sigma_{\rm add}$, respectively) for each data set are given in Table V.

A third source of systematic error may be caused by changes in detector efficiency with time, especially between the two polarized target states at each energy. Data collection with + and − target polarizations often were interrupted by periods of several to many hours, particularly during run period I. Detector gains could drift and efficiencies change in these periods between data collection. For example, when $C_0=1$ and $P_{T+}=P_{T-}=P_T$, then from Eqs. (7)

$$A_{ooon}=\frac{1}{P_T}\frac{n_{++}+n_{+-}-n_{-+}-n_{--}}{n_{++}+n_{+-}+n_{-+}+n_{--}}.$$

A change in detection efficiency in the elastic-scattering apparatus, so that

$$n_{++}^{\rm obs}=n_{++}^{\rm true}\times(1+\epsilon_e),$$

$$n_{+-}^{\rm obs}=n_{+-}^{\rm true}\times(1+\epsilon_e),$$

$$n_{-+}^{\rm obs}=n_{-+}^{\rm true}\times(1-\epsilon_e),$$

$$n_{--}^{\rm obs}=n_{--}^{\rm true}\times(1-\epsilon_e),$$

corresponding to an efficiency asymmetry ϵ_e, would then give

$$A_{ooon}^{\rm obs}=A_{ooon}^{\rm true}+\epsilon_e/P_T.$$

Similarly, a change in the efficiency of the beam intensity monitor AV would give

$$A_{ooon}^{\rm obs}=A_{ooon}^{\rm true}-\epsilon_b/P_T,$$

TABLE VI. Results from straight line fits to the A_{oon} data near 90° c.m. The beam kinetic energy, fitted slope, angle at zero crossing, and value at 90° are all presented. The 90° data include systematic errors. The values of χ^2 per degree of freedom for the weighted averages are 1.92 and 2.57, respectively.

Energy (MeV)	Slope ($\rm deg^{-1}$)	Angle (deg.)	A_{oon} (90°)
1795	−0.0101±0.0026	88.37±0.86	−0.0165±0.0083
1845	−0.0034±0.0021	88.23±2.03	−0.0061±0.0063
1935	−0.0029±0.0035	98.19±10.80	0.0235±0.0108
1955	−0.0123±0.0037	88.27±0.99	−0.0212±0.0113
1975	−0.0080±0.0025	88.85±0.94	−0.0092±0.0077
1995	−0.0159±0.0036	90.50±0.67	0.0079±0.0107
2015	−0.0076±0.0041	91.30±1.54	0.0099±0.0117
2035 I	−0.0074±0.0032	92.62±1.58	0.0194±0.0100
2035 II	−0.0063±0.0023	88.45±1.13	−0.0098±0.0069
2055	−0.0079±0.0031	90.91±1.18	0.0072±0.0093
2075	−0.0078±0.0028	89.15±1.05	−0.0067±0.0084
2095 I	−0.0111±0.0035	88.86±0.98	−0.0127±0.0108
2095 II	−0.0175±0.0024	88.51±0.40	−0.0260±0.0071
2115	−0.0107±0.0036	89.07±0.99	−0.0099±0.0106
2135	−0.0126±0.0034	89.35±0.83	−0.0082±0.0104
2155	−0.0149±0.0031	90.55±0.62	0.0082±0.0095
2175	−0.0127±0.0030	89.77±0.69	−0.0029±0.0091
2205	−0.0082±0.0038	86.40±2.30	−0.0297±0.0120
2215	−0.0113±0.0043	88.32±1.29	−0.0190±0.0124
2225	−0.0152±0.0035	91.53±0.73	0.0233±0.0105
2235	−0.0179±0.0048	91.59±1.12	0.0283±0.0155
Wt. Av.		89.51±0.19	−0.0047±0.0020

where ϵ_b is the monitor efficiency asymmetry, similar to ϵ_e above. In both cases, a shift in the values of A_{oon} would be caused.

This type of systematic error can be tested by evaluating A_{oon} at 90° c.m., where the value should be zero by the generalized Pauli principle [1]. The measured results within the range $90\pm5°$ were fit by a straight line; see Table VI. Since the data collection occurred in the pattern (E_1,P_{T+}), (E_1,P_{T-}), (E_2,P_{T-}), (E_2,P_{T+}), (E_3,P_{T+}), . . . for most of the run periods, a slow change in an efficiency would be expected to yield both positive and negative values of $A_{oon}(90°)$. The results suggest that the systematic errors are no larger than 0.03, and possibly much smaller. For example, the $A_{oon}(90°)$ results from Table VI are seen to be consistent with a slightly negative value averaging over all energies. It is concluded that there might have been a small error $(0.3-0.4°)$ in the measured laboratory angle, or about $(-0.5\pm0.2)°$ in the c.m. angle, for all energies. This is consistent with the estimated uncertainty in the absolute angle of $\pm0.18°$ lab. Note that the results from Table VI are plotted in Fig. 9 in Ref. [2], where these conclusions are reinforced.

IV. RESULTS

The $A_N=A_{oon}$ results for run periods I and II are given in Figs. 8–12 and Table V. A total of 19 different beam kinetic energies and 442 different points are included. Of the 21 data sets, four (1795, 1845, 2035 II, and 2095 II) were collected in the second run period, while the remaining sets were from run period I. At two beam energies, 2035 and 2095 MeV, there were repeated measurements. The figures show good agreement for the two run periods.

These new experimental data are also compared to previous results [18,28–34] in this angular and energy range in Figs. 8–12. Most of the data are in reasonably good agreement. The measurements at 1793–1796 MeV of Perrot *et al.* [18], 1958 MeV of Albrow *et al.* [28], 1967 MeV of Bell *et al.* [31], and 2205 MeV of Makdisi *et al.* [32] agree well with the data in this paper over the whole angular range, and of Miller *et al.* [29] at 2205 MeV except perhaps at the largest angles. Several of the existing data sets seem somewhat low near 70° c.m. but agree elsewhere. These include the measurements of Parry *et al.* [30] at 1967 MeV and 2138 MeV, and Perrot *et al.* [18] at 2093–2096 MeV. Two points of Diebold *et al.* [33] at 2205 MeV are shown. The data of Neal and Longo [34] at 2240 MeV are considerably below the results from this paper. A global analysis of pp analyzing power data for $|t|\leqslant0.7\,\mathrm{GeV}^2/c^2$ was performed some time ago [35]. This analysis studied the Zero-Gradient Synchrotron beam polarimeters, and it concluded that the data of Refs. [30,33] should be renormalized upward by 15 and 10%, respectively, and of Ref. [31] should be renormalized downward by 8%; no changes were suggested for Refs. [28,29,34]. These suggested changes would improve the agreement with the new data from this paper.

Two recent phase-shift analyses (PSA) have been performed in the range of the measurements reported in this paper. The Saclay-Geneva PSA [36] occurs at four energies (1.8, 2.1, 2.4, and 2.7 GeV) using previous data and the present results near these energies. The Arndt *et al.* PSA [37] has recently been extended from 1.6 to 2.5 GeV, and includes all the data from this paper. The two PSA predictions are compared to data at 1795 and 2095 MeV in Figs. 8 and 10, and the Arndt *et al.* predictions at a selection of other energies are given in Figs. 8–12. Quite good agreement occurs at all energies, because the present results are in the two PSA data bases, and also agree well with previous measurements near 1.8 and 2.1 GeV. The present data and results from [5–7] improve the direct reconstruction of the pp scattering amplitudes at the four energies 1.8, 2.1, 2.4, and 2.7 GeV [36].

The large number of new data points from this paper, in an energy region that was previously covered only sparsely, will make a significant contribution to the knowledge of the nucleon-nucleon elastic-scattering amplitudes. Considerable care was taken to minimize systematic errors in these measurements from changes in detector efficiencies or operating conditions.

ACKNOWLEDGMENTS

We wish to express our gratitude to C. Lechanoine-Leluc and J. Comfort for encouraging suggestions. For excellent operation of the Saturne II accelerator, we are indebted to all of the operations staff. This work was supported in part by the U.S. Department of Energy, Division of Nuclear Physics, Contract No. W-31-109-ENG-38, by the Swiss National Science Foundation, and by the Russian Foundation for Fundamental Nuclear Physics Program 122.03.

[1] J. Bystricky, F. Lehar, and P. Winternitz, J. Phys. (Paris) **39**, 1 (1978).

[2] C. E. Allgower, J. Ball, M. E. Beddo, J. Bystricky, P. A. Chamouard, M. Combet, Ph. Demierre, J.-M. Fontaine, D. P. Grosnick, R. Hess, Z. Janout, Z. F. Janout, V. A. Kalinnikov, T. E. Kasprzyk, B. A. Khachaturov, R. Kunne, F. Lehar, A. de Lesquen, D. Lopiano, M. de Mali, V. N. Matafonov, I. L. Pisarev, A. A. Popov, A. N. Prokofiev, D. Rapin, J. L. Sans, H. M. Spinka, A. Teglia, Yu. A. Usov, V. V. Vikhrov, B. Vuaridel, and A. A. Zhdanov, Phys. Rev. C **60**, 054002 (1999), following paper.

[3] C. E. Allgower, Ph.D. thesis, Arizona State University and Argonne National Laboratory report ANL-HEP-TR-97-71, 1997.

[4] J. Ball, P. A. Chamouard, M. Combet, J. M. Fontaine, R. Kunne, J. M. Lagniel, J. L. Lemaire, G. Milleret, J. L. Sans, J. Bystricky, F. Lehar, A. de Lesquen, M. de Mali, Ph. Demierre, R. Hess, Z. F. Janout, E. L. Lomon, D. Rapin, B. Vuaridel, L. S. Barabash, Z. Janout, V. A. Kalinnikov, Yu. M. Kazarinov, B. A. Khachaturov, V. N. Matafonov, I. L. Pisarev, A. A. Popov, Yu. A. Usov, M. Beddo, D. Grosnick, T. Kasprzyk, D. Lopiano, H. Spinka, A. Boutefnouchet, V. Ghazikhanian, and

C. A. Whitten, Phys. Lett. B **320**, 206 (1994).

[5] C. E. Allgower, J. Ball, L. S. Barabash, M. Beddo, Y. Bedfer, A. Boutefnouchet, J. Bystricky, Ph. Demierre, J.-M. Fontaine, V. Ghazikhanian, D. Grosnick, R. Hess, Z. Janout, Z. F. Janout, V. A. Kalinnikov, T. E. Kasprzyk, Yu. M. Kazarinov, B. A. Khachaturov, R. Kunne, F. Lehar, A. de Lesquen, D. Lopiano, M. de Mali, V. N. Matafonov, I. L. Pisarev, A. A. Popov, A. N. Prokofiev, D. Rapin, J.-L. Sans, H. M. Spinka, S. Trentalange, Yu. A. Usov, V. V. Vikhrov, B. Vuaridel, C. A. Whitten, and A. A. Zhdanov, Eur. Phys. J. C **1**, 131 (1998).

[6] C. E. Allgower, J. Ball, M. Beddo, Y. Bedfer, A. Boutefnouchet, J. Bystricky, P.-A. Chamouard, Ph. Demierre, J.-M. Fontaine, V. Ghazikhanian, D. Grosnick, R. Hess, Z. Janout, Z. F. Janout, V. A. Kalinnikov, T. E. Kasprzyk, B. A. Khachaturov, R. Kunne, F. Lehar, A. de Lesquen, D. Lopiano, V. N. Matafonov, I. L. Pisarev, A. A. Popov, A. N. Prokofiev, D. Rapin, J.-L. Sans, H. M. Spinka, A. Teglia, Yu. A. Usov, V. V. Vikhrov, B. Vuaridel, C. A. Whitten, and A. A. Zhdanov, Nucl. Phys. **A637**, 231 (1998).

[7] C. E. Allgower, J. Ball, L. S. Barabash, M. Beddo, Y. Bedfer, A. Boutefnouchet, J. Bystricky, P.-A. Chamouard, Ph. Demierre, J.-M. Fontaine, V. Ghazikhanian, D. Grosnick, R. Hess, Z. Janout, Z. F. Janout, V. A. Kalinnikov, T. E. Kasprzyk, Yu. M. Kazarinov, B. A. Khachaturov, R. Kunne, C. Lechanoine-LeLuc, F. Lehar, A. de Lesquen, D. Lopiano, M. de Mali, V. N. Matafonov, I. L. Pisarev, A. A. Popov, A. N. Prokofiev, D. Rapin, J.-L. Sans, H. M. Spinka, Yu. A. Usov, V. V. Vikhrov, B. Vuaridel, C. A. Whitten, and A. A. Zhdanov, Eur. Phys. J. C **5**, 453 (1998).

[8] J. Ball, C. E. Allgower, M. Beddo, J. Bystrický, M. Combet, Ph. Demierre, G. Durand, J.-M. Fontaine, D. Grosnick, R. Hess, Z. Janout, Z. F. Janout, V. A. Kalinnikov, T. E. Kasprzyk, B. A. Khachaturov, R. Kunne, F. Lehar, A. de Lesquen, D. Lopiano, V. N. Matafonov, I. L. Pisarev, A. A. Popov, A. N. Prokofiev, D. Rapin, J.-L. Sans, H. M. Spinka, Yu. A. Usov, V. V. Vikhrov, B. Vuaridel, and A. A. Zhdanov, Eur. Phys. J. C (submitted).

[9] J. Arvieux, in *Polarized Proton Ion Sources*, Ann Arbor, 1981, edited by A. D. Krisch and A. T. M. Lin, AIP Conf. Proc. No. 80 (AIP, New York, 1982), p. 185.

[10] J. Arvieux, S. D. Baker, R. Beurtey, M. Boivin, J. M. Cameron, T. Hasegawa, D. Hutcheon, J. Banaigs, J. Berger, A. Codino, J. Duflo, L. Goldzahl, F. Plouin, A. Boudard, G. Gaillard, N. Van Sen, and Ch. F. Perdrisat, Nucl. Phys. **A431**, 613 (1984).

[11] J. Arvieux, S. D. Baker, A. Boudard, J. Cameron, T. Hasegawa, D. Hutcheon, C. Kerboul, G. Gaillard, and N. Van Sen, Nucl. Instrum. Methods Phys. Res. A **273**, 48 (1988).

[12] J. Arvieux in *Eighth International Symposium on High-Energy Spin Physics*, Minneapolis, 1988, edited by K. J. Heller, AIP Conf. Proc. No. 187 (AIP, New York, 1989), p. 1191.

[13] P.-A. Chamouard, J.-M. Lagniel, J.-L. Lemaire, A. Tkatchenko, and J. Yonnet, J. Phys. (Paris), Colloq. **51**, C6-569 (1990).

[14] J.-L. Lemaire, Proceedings of the International Workshop on Polarized Sources and Polarized Gas Jets, edited by Y. Mori, KEK Report 90-15, Tsukuba, Japan, p. 116, 1990.

[15] C. E. Allgower, J. Arvieux, P. Ausset, J. Ball, P.-Y. Beauvais, Y. Bedfer, J. Bystricky, P.-A. Chamouard, P. Demierre, J.-M. Fontaine, Z. Janout, V. A. Kalinnikov, T. E. Kasprzyk, B. A. Khachaturov, R. Kunne, J.-M. Lagniel, F. Lehar, A. de Lesquen, A. A. Popov, A. N. Prokofiev, D. Rapin, J.-L. Sans, H. M. Spinka, A. Teglia, V. V. Vikhrov, B. Vuaridel, and A. A. Zhdanov, Nucl. Instrum. Methods Phys. Res. A **399**, 171 (1997).

[16] J. Bystricky, P. Chaumette, J. Derégel, J. Fabre, F. Lehar, A. de Lesquen, F. Petit, L. van Rossum, J. M. Fontaine, F. Perrot, J. Ball, A. Michalowicz, Y. Onel, and A. Penzo, Nucl. Phys. **B262**, 715 (1985).

[17] J. Bystricky, P. Chaumette, J. Derégel, J. Fabre, F. Lehar, A. de Lesquen, L. van Rossum, J. M. Fontaine, J. Gosset, F. Perrot, C. A. Whitten, J. Ball, Ph. Chesny, C. R. Newsom, J. Yonnet, T. Niinikoski, M. Rieubland, A. Michalowicz, and S. Dalla Torre-Colautti, Nucl. Phys. **B262**, 727 (1985).

[18] F. Perrot, J. M. Fontaine, F. Lehar, A. de Lesquen, J. P. Meyer, L. van Rossum, P. Chaumette, J. Derégel, J. Fabre, J. Ball, C. D. Lac, A. Michalowicz, Y. Onel, B. Aas, D. Adams, J. Bystricky, V. Ghazikhanian, G. Igo, F. Sperisen, C. A. Whitten, and A. Penzo, Nucl. Phys. **B294**, 1001 (1987).

[19] F. Lehar, A. de Lesquen, J. P. Meyer, L. van Rossum, P. Chaumette, J. Derégel, J. Fabre, J. M. Fontaine, F. Perrot, J. Ball, C. D. Lac, A. Michalowicz, Y. Onel, D. Adams, J. Bystricky, V. Ghazikhanian, C. A. Whitten, and A. Penzo, Nucl. Phys. **B294**, 1013 (1987).

[20] C. D. Lac, J. Ball, J. Bystricky, J. Derégel, F. Lehar, A. de Lesquen, L. van Rossum, J. M. Fontaine, F. Perrot, and P. Winternitz, J. Phys. (France) **51**, 2689 (1990), and references contained therein.

[21] J. Bystricky, J. Derégel, F. Lehar, A. de Lesquen, L. van Rossum, J. M. Fontaine, F. Perrot, C. A. Whitten, T. Hasegawa, C. R. Newsom, W. R. Leo, Y. Onel, S. Dalla Torre-Colautti, A. Penzo, H. Azaiez, and A. Michalowicz, Nucl. Instrum. Methods Phys. Res. A **239**, 131 (1985).

[22] R. Bernard, P. Chaumette, P. Chesny, J. Derégel, R. Duthil, J. Fabre, C. Lesmond, G. Seité, J. Ball, T. O. Niinikoski, and M. Rieubland, Nucl. Instrum. Methods Phys. Res. A **249**, 176 (1986).

[23] J. Ball, M. Combet, J.-L. Sans, B. Benda, P. Chaumette, J. Derégel, G. Durand, A. P. Dzyubak, C. Gaudron, F. Lehar, A. de Lesquen, T. E. Kasprzyk, Z. Janout, B. A. Khachaturov, V. N. Matafonov, and Yu. A. Usov, Nucl. Instrum. Methods Phys. Res. A **381**, 4 (1996).

[24] A. Abragam and M. Goldman, *Nuclear Magnetism: Order and Disorder* (Clarendon, Oxford, 1982); Rep. Prog. Phys. **41**, 395 (1978).

[25] M. Arignon, J. Bystricky, J. Derégel, F. Lehar, A. de Lesquen, F. Petit, L. van Rossum, J. M. Fontaine, F. Perrot, J. Ball, and C. D. Lac, Nucl. Instrum. Methods Phys. Res. A **262**, 207 (1987).

[26] J. Ball, Ph. Chesny, M. Combet, J. M. Fontaine, R. Kunne, J. L. Sans, J. Bystricky, C. D. Lac, D. Legrand, F. Lehar, A. de Lesquen, M. de Mali, F. Perrot-Kunne, L. van Rossum, P. Bach, Ph. Demierre, G. Gaillard, R. Hess, Z. F. Janout, D. Rapin, Ph. Sormani, B. Vuaridel, J. P. Goudour, R. Binz, A. Klett, E. Rössle, H. Schmitt, L. S. Barabash, Z. Janout, V. A. Kalinnikov, Yu. M. Kazarinov, B. A. Khachaturov, V. N. Matafonov, I. L. Pisarev, A. A. Popov, Yu. A. Usov, M. Beddo, D. Grosnick, T. Kasprzyk, D. Lopiano, and H. Spinka,

Nucl. Instrum. Methods Phys. Res. A **327**, 308 (1993).
[27] S. Brehin, D. Lascols, and P. Briet, DPhPE, CEN-Saclay internal report, 1980.
[28] M. G. Albrow, S. Andersson/Almehed, B. Bošnjaković, C. Daum, F. C. Erné, J. P. Lagnaux, J. C. Sens, and F. Udo, Nucl. Phys. **B23**, 445 (1970).
[29] D. Miller, C. Wilson, R. Giese, D. Hill, K. Nield, P. Rynes, B. Sandler, and A. Yokosawa, Phys. Rev. D **16**, 2016 (1977).
[30] J. H. Parry, N. E. Booth, G. Conforto, R. J. Esterling, J. Scheid, D. J. Sherden, and A. Yokosawa, Phys. Rev. D **8**, 45 (1973).
[31] D. A. Bell, J. A. Buchanan, M. M. Calkin, J. M. Clement, W. H. Dragoset, M. Furić, K. A. Johns, J. D. Lesikar, H. E. Miettinen, T. A. Mulera, G. S. Mutchler, G. C. Phillips, J. B. Roberts, and S. E. Turpin, Phys. Lett. **94B**, 310 (1980).
[32] Y. Makdisi, M. L. Marshak, B. Mossberg, E. A. Peterson, K. Ruddick, J. B. Roberts, and R. D. Klem, Phys. Rev. Lett. **45**, 1529 (1980).
[33] R. Diebold, D. S. Ayres, S. L. Kramer, A. J. Pawlicki, and A. B. Wicklund, Phys. Rev. Lett. **35**, 632 (1975).
[34] H. A. Neal and M. J. Longo, Phys. Rev. **161**, 1374 (1967).
[35] H. Spinka, E. Colton, W. R. Ditzler, H. Halpern, K. Imai, R. Stanek, N. Tamura, G. Theodosiou, K. Toshioka, D. Underwood, R. Wagner, Y. Watanabe, A. Yokosawa, G. R. Burleson, W. B. Cottingame, S. J. Greene, S. Stuart, and J. J. Jarmer, Nucl. Instrum. Methods Phys. Res. **211**, 239 (1983).
[36] J. Bystrický, C. Lechanoine-LeLuc, and F. Lehar, Eur. Phys. J. C **4**, 607 (1998).
[37] R. A. Arndt, C. H. Oh, I. I. Strakovsky, R. L. Workman, and F. Dohrmann, Phys. Rev. C **56**, 3005 (1997); SAID solution SP99.